Internal Diameter Coating by Warm Spraying of Fine WC-12Co Powders (− 10 + 2 μm) with Very Short Spray Distances up to 10 mm

I. Baumann[1] · W. Tillmann[1] · C. Schaak[1] · K. Schmidt[1] · L. Hagen[1] · J. Zajaczkowski[1] · G. Schmidtmann[1] · G. Matthäus[2] · W. Luo[2]

Abstract The internal diameter (ID) coating by means of thermal spraying is currently experiencing growing interest in science and industry. In contrast to the well-established plasma- and arc-based spray techniques, there is a lack of knowledge concerning kinetic processes such as HVOF, HVAF and warm spray (WS). A major challenge represents the necessity of short spray distances and the compact design of novel ID spray guns with reduced combustion power. Conventional WC-Co powders (− 45 + 15 μm) are not able to achieve a sufficient heat and momentum transfer. The use of fine powders < 15 μm offers an approach to overcome this drawback as they feature a larger surface-to-volume ratio and a lower mass. However, the processing of fine powders requires suitable spray equipment and a sensitive parameter adjustment. In this study, warm spraying of fine WC-12Co powders (− 10 + 2 μm) with a novel ID spray gun (HVOF + N₂) "ID RED" (Thermico Engineering GmbH, Germany) was investigated. First, the flame profile as well as the in-flight behavior of the particles along the spray jet (spray distances SD = 10-80 mm) was analyzed at different nitrogen flows NF = 15-115 L/min to find suitable spray parameter intervals. Subsequently, planar steel samples were coated with SD = 10-50 mm and constant NF = 90 L/min. Analyses regarding the microstructure, the mechanical properties and the phase evolution of the coatings were performed. The aim was to study spraying with the novel ID gun and to scrutinize shortest feasible spray distances.

Finally, steel tubes (internal diameter of 81.6 mm and a wall thickness of 10.0 mm) were coated with SD = 20 mm and NF = 90 L/min to investigate in how far the results can be transferred to ID parts. Correlations between the particle behavior, the microstructure and the coating properties were made.

Introduction

Atmospheric plasma spraying (APS), twin-wire arc spraying (TWAS), plasma transferred wire arc spraying (PTWA) and rotating single-wire (RSW) spraying are among the well-established processes for the coating of parts with inner surfaces (ID coating). They are particularly used in the automotive industry to coat cylinder bores of light metal cast engine blocks to mitigate wear and friction, thus improving the engine efficiency (Ref 1). Other typical ID components are tubes, pipe elbows, shock struts of landing gears, hydraulic actuators, bearings, crankshafts, nozzles, oil refinery sleeves, barrels, inside bores or pump parts.

In contrast to the arc- and plasma-based techniques, kinetic spray processes such as HVOF, HVAF and warm spray (WS) have hardly been scientifically investigated for the coating of inner surfaces and are not well established in industry for this purpose (Ref 2, 3). These spray processes are based on supersonic gas jets achieved by the combustion and expansion of a liquid (LF) or gaseous (GF) fuel (hydrogen or hydrocarbons) together with oxygen (HVOF), compressed air (HVAF) or additional nitrogen gas (WS) in a convergent–divergent nozzle (Ref 4). Depending on the

✉ I. Baumann
ingor.baumann@tu-dortmund.de

1 Institute of Materials Engineering, Technische Universität Dortmund, Dortmund, Germany

2 Thermico Engineering GmbH, Dortmund, Germany

type of fuel, the powder feedstock is fed into the spray gun either radially (LF systems) or axially (GF systems) (Ref 5, 6). In LF systems, the powder particles are fed into the colder section of the process gas flow between the converging–diverging part of the nozzle instead of being fed directly into combustion chamber as in GF systems. This effectively reduces overheating of the powder particles (Ref 7). Most of the GF systems provide higher particle temperatures than LF ones, while the latter are characterized by higher particle velocities due to more momentum output (Ref 7, 8). Thus, LF systems generate denser coating structures with less thermal phase reactions and better bonding to the substrate in comparison with GF systems (Ref 9).

The HVAF technology is a further development of HVOF, which was originally introduced to minimize the operating costs associated with the use of pure oxygen and to increase the flexibility of the HVOF processes through higher particle velocities and lower spray temperatures (Ref 10-12). According to Katanoda et al, the gas temperature in the HVAF process is around 1000 K lower than in the HVOF (Ref 13). The authors also indicated that in both processes (HVOF and HVAF), the gas temperature can be controlled in a narrow range of around 300 K by changing the equivalence ratio in the combustion chamber. Since the original composition and microstructure of the powder can largely be retained in HVAF cermet coatings, they are not only denser and more homogeneous than HVOF ones, but also feature less oxidation and improved toughness. Therefore, HVAF-sprayed cermet coatings generally achieve a better wear performance (Ref 14-16).

Warm spray (WS) represents a more recent modification of HVOF spraying (Ref 17). First related studies were published in 2006 (Ref 18, 19). During warm spraying, the temperature of the propellant gas can be effectively controlled in the range of 500-2000 °C and the gas velocity between 900 and 1600 m/s by injecting nitrogen gas with different volume flows into the combustion chamber (Ref 20-25). In analogy to cold gas spraying (CGS), the WS process is also based on high-velocity impact bonding of powder particles, but the impact temperature of the spray particles is higher and often close to the melting point of the material(Ref 17). Therefore, WS is often regarded as a spray process between CS and HVOF. The specific properties of WS ensure, on the one hand, a sufficient deformability of the spray particles during deposition (from the solid or semi-melting state) (Ref 26). On the other hand, the particles are moderately heated and thermally softened (Ref 22). Thus, the risk of an overheating of the spray particles can be significantly reduced, making WS particularly suitable for the processing of heat- or oxygen-sensitive materials (Ref 20, 27). In addition, higher gas

pressures in the combustion chamber, resulting from higher gas mass flows and the thermal expansion of the nitrogen gas during heating, also promote higher particle velocities (Ref 2). Several authors reported that detrimental phase reactions such as oxidization and decarburization could be entirely suppressed by warm spraying of WC-Co powders (Ref 21, 23, 24, 28, 29). The corresponding coatings showed no or little formation of W_2C and η phases and also feature moderately improved fracture properties for WC-Co coatings when higher cobalt contents such as 17 and 25 wt.% were used (Ref 22, 28). Further benefits of warm sprayed WC-Co coatings are higher hardness, more homogeneous and finer microstructures as well as a better surface quality compared to other kinetic spray processes like HVOF and HVAF (Ref 17).

In the field of OD (outer diameter) coating, kinetic spray processes with WC-Co(Cr) or Cr_3C_2-NiCr as powder feedstock in conventional size fractions from 15 to 45 μm have been used for decades to protect applications from wear and corrosion. Latest generation of kinetic spray process can produce very dense coating structures due to the higher kinetic energy (Ref 30). Since the benefits of such coatings over other spray techniques are numerous (Ref 31), they are particularly interesting for the ID coating. However, the ID coating of parts, particularly with small internal diameters < 125 mm (Ref 32), is a challenging process. Many fundamental mechanisms have not been scientifically investigated and clarified so far. The process-specific effort increases significantly with the reduction in the diameter and with rising geometric complexity of the inner surfaces. The ID coating of parts with small internal diameters makes the use of novel spray processes and shorter spray distances of 50 mm or less indispensable. Special ID-HVOF, HVAF and WS guns with more compact combustion chamber design and shorter (L-shaped) nozzles than traditional guns are available on the market by now. The combustion power of these ID spray guns is much lower, leading to shorter and more narrow spray plumes with lower thermal and kinetic energy. It is well known that the temperature and velocity of the process gas flow associated with the dwell time of the spray particles passing through the flame strongly determine their acceleration and melting behavior (Ref 2). Beside the combustion parameters, the length of the nozzle (barrel) and the spray distance are majorly important factors controlling the dwell time (Ref 33). Due to the high jet velocity of kinetic spray process, the dwell time generally needs to be maximized by large spray distances to achieve a sufficient plastic particle deformation when they hit the substrate surface and to enable an appropriate bonding. However, spraying at very short spray distances using compact, low-energy ID spray guns lead to very short

dwell times in which conventional WC-Co spray powders cannot experience a sufficient heat and momentum transfer.

The use of fine WC-Co spray powders with agglomerate sizes < 15 μm composed of individual WC and matrix particles within the submicron or nano range represents a way to overcome this drawback. Due to their larger specific surface and lower mass, fine powders can interact more intensely with the hot spray jet than larger ones (Ref 32). This enables a rapid particle heating and promotes achieving a thermal equilibrium. Furthermore, fine powders are able to follow the gas flow trajectories better than larger particles (Ref 34), thus reaching higher particle velocities than conventional powders. These capabilities enable fine powders to achieve a sufficient acceleration and melting despite short spray distances and low combustion powers of the ID spray guns. However, due to their poor flowability, high tendency to agglomerate and thermal susceptibility, ID spraying of fine WC-Co powders imposes new challenges. Appropriate powder handling and spray equipment as well as a careful adjustment of the spray parameter settings are essential. Since warm spraying allows to control the process gas temperatures sensitively, this technique is particularly suitable for the processing of fine powders. Despite the availability of novel kinetic ID spray systems, which principally allow the coating of parts with small inner radii < 125 mm, there is a lack of knowledge about the possibilities and limits using fine WC-Co powders for the ID coating.

In this study, warm spraying of fine WC-12Co powders (− 10 + 2 μm) with a novel ID spray gun "ID RED" (Thermico Engineering GmbH, Germany) was investigated. First, the stability and the profile of the flame (in terms of length and width) as well as the in-flight behavior of the particles (i.e., temperature and velocity) along the spray jet were analyzed at spray distances from SD = 10 mm to SD = 80 mm and varying nitrogen flows from NF = 15 to 115 L/min to identify suitable spray parameter intervals. Subsequently, planar steel samples were coated at spray distances between SD = 10 mm and SD = 50 mm and a constant nitrogen flow of NF = 90 L/min. Analyses regarding microstructure, mechanical properties and phase evolution of the coatings were performed. The aim was to investigate the coating development by means of the novel ID spray gun and fine WC-12Co powders. In addition, shortest feasible spray distances for coating should be found. The results were compared with finely structured WC-12Co OD (outer diameter) coatings. Finally, steel tubes with an internal diameter of 81.6 mm were coated on the inner side to investigate in how far the results can be transferred to ID parts. Correlations between particle behavior, microstructure and coating properties were carried out.

Experimental

Substrate

The finely structured WC-12Co coatings were firstly applied to planar samples (35 mm × 50 mm × 10 mm) and afterward to the inner surfaces of seamlessly drawn tubes (inner diameter 81.6 mm, wall thickness 10.0 mm), both made of unalloyed structural steel (1.0576). Prior to the coating operation, the substrates were grit blasted with pure corundum at an angle of 45° and a spray distance of 100 mm. EKF100 corundum grits (106-150 μm) and a blasting pressure of 2 bar were used for the planar samples. This provided a medium surface roughness of Ra = 1.42 ± 0.11 μm. Due to the manufacturing process, the inner surface of the tubes is of lower quality than the planar samples. These were therefore blasted in two steps to reduce draw marks and unevenness: first with EKF14 corundum (1180-1700 μm) at 3 bar and afterward with EKF60 corundum (212-300 μm) at 4 bar. All specimens were subsequently cleaned in an ethanol ultrasonic bath and preheated to reduce thermal stress during coating.

Powder Feedstock

A fine, agglomerated and sintered WC-12Co powder of mainly spherical shape (Type DURMAT 131.046, Durum Verschleißschutz, Germany) was used as feedstock. The size fraction of the agglomerates is − 10 + 2 μm, and the submicron WC particles have an average Fisher sub-sieve grain size of 400 nm. According to the manufacturer, the powder is composed of the following elements in weight percent: C 5.51 %, Co 12.54 %, W balance, Fe < 0.1 %, Ni 0.01 %, no oxygen.

Powder Analyses

A S3500 laser diffraction system (Microtrac, USA) was used to measure the agglomerate-size distribution of the powder. The flowability of the fine powder was too low and could not be determined by a conventional Hall tester/flow meter. Instead, the dynamic flow behavior was determined with a Revolution Powder Analyzer (RPA, Mercury Scientific Inc., Newtown, USA) by analyzing the sequence and the behavior of avalanches within the RPA test with low rotation speed of the drum (Ref 35, 36). This measuring procedure is often used to ascertain the flowability of powders for additive manufacturing processes (Ref 36). For this purpose, the avalanche angle, the power of avalanches (i.e., the avalanche energy) and the numbers of avalanches were investigated. The avalanche energy is the amount of energy released by an avalanche in the powder

test portion. It is calculated by subtracting the energy level of the powder after an avalanche from the energy level before. Powders with high flowability are characterized by performing a large number of avalanches at low avalanche energies (Ref 37). The avalanche angle defines the angle of a linear regression of the free powder surface at the position of maximum potential energy just before an avalanche starts, measured to a horizontal line (Ref 36). The higher the avalanche angle, the lower the flowability of the powder. A further description of this measuring system is given elsewhere (Ref 37). The flowability tests were performed with a 100 cm^3 test portion of the fine powder at a drum rotation speed of 1.0 rpm and a frame rate of 20 fps.

Spray Process

All spray experiments were carried out with the ID RED spray gun (Thermico Engineering GmbH, Germany), which is optimized for the processing of fine or heat-sensitive powders (Ref 38). This is a liquid cooled HVOF + N$_2$ (warm spray) system with single radial powder injection. It uses a hydrogen-stabilized kerosene-oxygen combustion as energy source and offers the option to inject variable nitrogen gas flows (NF = 0-150 L/min) into the combustion chamber. The system has a compact and angled (L-shaped) design and is capable of coating inner surfaces with a minimum internal diameter of 63 mm (Ref 38). Kerosene volume flows of up to 4 L/h can be realized, whereby the system provides a low combustion power of 5-35 kW and chamber pressures of 6-14 bar. Due to the required redirection of the process gas flow, the angle between the gun shaft and the flame jet is 82°. While the convergent section of the de Laval system is part of the combustion chamber, the nozzle (barrel) forms the divergent part. An L-shaped bend, which is located between combustion chamber and the nozzle, diverts the process gas flow into the nozzle. The nozzle consists of a cemented carbide socket that is brazed into a copper jacket. It has a total length of 16 mm, whereby the bore diameter tapers from initially 5 mm (entry of the process gas flow from the combustion chamber via the bend) to 6 mm (at the process gas flow exit). The powder is fed radially into the gun by means of an injector in the middle part of the nozzle.

Commercially available kerosene (EXXSOL D60, ExxonMobil Chemical, USA) was used as liquid fuel. The powder was fed into the ID gun by means of a CPF2-Twin fine powder feeder system (Thermico Engineering GmbH, Germany) according to the gravimetric dosing mode by means of an internal weighing equipment. To ensure a continuous powder flow, the containers of the feeder system were heated to 80 °C and agitated with a vibrator device at a pressure of 5 bar. Nitrogen was used as carrier gas. The spray and motion parameter settings for the

Table 1 Spray and motion parameter settings for the coating of planar steel samples and steel tubes

Parameter	Planar samples	Tubes
Kerosene flow KF, L/h	2.5	2.5
Oxygen/fuel ratio λ	1.2	1.2
Oxygen flow OF, L/min	130	130
Hydrogen flow HF, L/min	110	110
Carrier gas flow CGF, L/min	6	6
Nitrogen flow NF, L/min	90	90
Powder flow PF, g/min	20	20
Spray distance SD, mm	10; 20; 30; 40; 50	20
Gun velocity GV, m/min	3,000	.
Rotation velocity RV, 1/min	.	115.8
Axial (feed) velocity AV, mm/min	.	231.5
Track pitch TP, mm	2	2
Coating depth CD, mm	.	50
Number of passes NP	20	20
Air cooling pressure ACP, bar	.	4

industrial robot system, which were varied according to the "one-factor-at-a-time" (OFAT) method and used for the coating of planar steel samples and steel tubes, are summarized in Table 1. These parameters were selected according to the manufacturer's recommendations as well as some preliminary tests, in which the basic processing of fine WC-Co powders using the ID RED warm spray gun was investigated. The spray distance (SD), which is one of the most important influencing factors in internal coating, was selected in the ranges typical for ID spraying (SD = 30 to 50 mm). In addition, spraying at very short spray distances of SD = 10 to 20 mm was also investigated to determine the potentials and limits of the ID coating using the above-mentioned gun system. When selecting the spray parameters, special attention was paid to the nitrogen flow (NF), as this has a strong influence on the thermo-kinetic behavior of fine WC-Co spray particles in the flame. For this purpose, the process stability and the particle behavior in-flight (i.e., particle velocity and temperature) along the flame axis with a large NF interval were analyzed. A medium NF of 90 L/min was then selected for the subsequent coating deposition on the planar samples and the steel tubes, since a stable process as well as a high particle velocity and a moderate particle temperature were achieved at this value. Photographs of the experimental setup for the coating of the planar samples and tubes are given in Fig. 1.

Flame Stability, Flame Profile Analysis and Particle Diagnostics

The in-flight behavior of the particles during warm spraying of fine WC-12Co powders was investigated by means
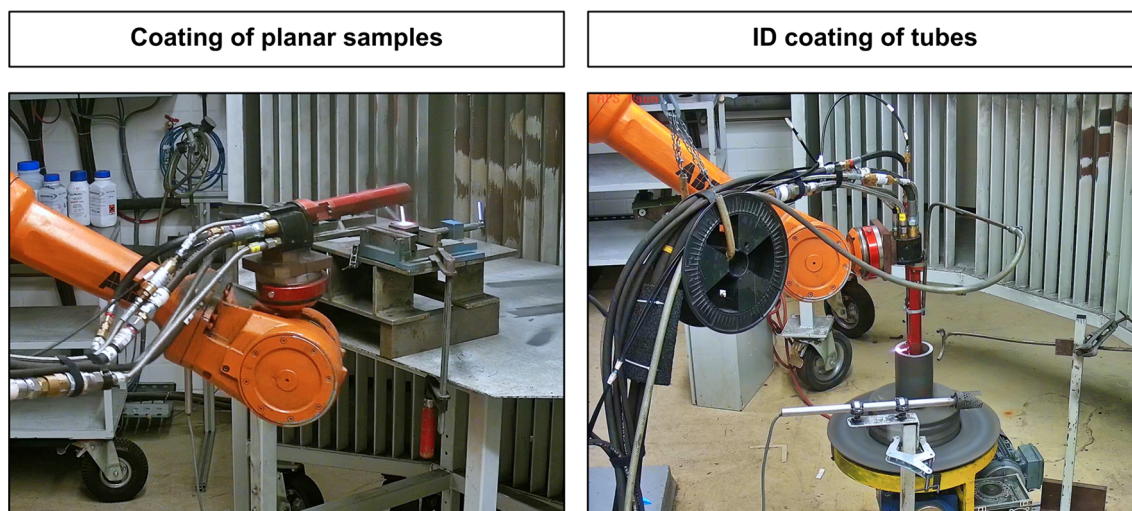
Coating of planar samples	ID coating of tubes

Fig. 1 Experimental setup for the ID coating process

of an Accuraspray-g3 device (Tecnar, Canada) using a low-emission head. During these analyses, the influence of different nitrogen flows (NF = 15, 40, 65, 90 and 115 L/min) on the profile (i.e., length and widths) and the stability of the particle-laden flame as well as on the particle temperature and velocity was scrutinized. For this purpose, examinations at different spray distances (SD = 10, 20, 30, 40, 50, 60, 70 and 80 mm) for the respective nitrogen flows were performed according to the "one-factor-at-a-time" (OFAT) method. At least three analyses with a minimum time of 30 seconds were performed for each measured value, and the mean value was then calculated from them for a total of 120 measurements. The shutter speed was set to 1/125 and the amplification to 128x. The Accuraspray-g3 device uses a two-color pyrometer sensor to determine the particle temperature, whereas the particle velocity is measured by means of a cross-correlation. Further information on the device and the measuring principle can be found in other studies, for instance in (Ref 39).

To measure the particle-laden flame length, the spray gun was positioned in front of a measuring device (ruler) immediately after each coating experiment, with the barrel exit positioned at the zero point of the ruler. The flame stability and development at different nitrogen flows was recorded in videos for a minimum of 30 seconds, and the flame length was evaluated by image analysis. The flame width was determined by analyzing the plume profile data recorded by the Accuraspray-g3 device.

Phase Analysis

The phase composition of the WC-Co power feedstock and the warm sprayed WC-12Co coatings on planar samples

was determined by means of x-ray diffraction (XRD) using a Bruker Advanced D8 diffractometer (Bruker AXS, Wisconsin) equipped with a 1-mm point focus polycap optic and Cu Kα radiation (λ = 1.5406 Å) which corresponds to a photon energy of 8.048 keV. The tube voltage and current were set to 40 kV and 30 mA, respectively. The scans were performed in locked couple mode in a scattering angle (2θ) range from 25° to 125°. The step width and exposure time for each step were set to 0.025° and 1 s, respectively. The diffracted intensity pattern is simultaneously recorded in a 2θ angular range from 30° to 50° using a step width and exposure time of 0.025° and 2.5 s. To measure the scattered intensity, a LYNXEYE XE detector system (Bruker AXS, Wisconsin, USA) was utilized. The phase composition was afterward ascertained using the software EVA Diffrac Plus (Bruker AXS, Wisconsin, USA) in conjunction with a reference database (i.e., Crystallography Open Database).

Coating Characterization

Cross-sectional images of the coating were taken by a light microscope (type Axiophot, Zeiss, Germany, and type BX51M, Olympus Germany) as well as a FESEM with secondary-electron (SE) and backscattered electron (BSE) detectors type JSM-7001F (JEOL, Germany). An equipped EDS device (INCAx-act, Oxford, UK) was used for the analysis of the elements. The coating thickness and porosity were determined by means of digital image analysis (software Axiovision Autmess, Zeiss, Germany). Vickers microhardness measurements were conducted with a load of 2.94 N (HV 0.3) along the cross section of the coating using a microhardness tester (NEXUS 400, Innovatest, The Netherlands). A tactile measurement machine

(Hommel Tester T1000/TK300, Hommelwerke, Germany) was used to determine the roughness Ra of the coating surface. The deposition efficiency (DE) was calculated based on the powder flow and the deposited coating mass. By measuring the length of Palmqvist cracks on HV 2.5 indentations in the center of the coating cross section and evaluating them according to the method of Shetty et al. (Ref 40, 41), the fracture toughness (K_{lc}) was determined.

Results and Discussion

Powder Size and Morphology Analysis

Figure 2 shows SEM images of the employed fine WC-12Co powder in top view (Fig. 2a) and in cross-sectional view (Fig. 2b) as well as the volume-based frequency distribution and cumulative size distribution of the WC-Co agglomerates (Fig. 2c). As these images and further SEM investigations reveal, the powder has a nearly spherical shape. The cross-sectional image of the agglomerate shows both dense areas of closely interconnected WC and Co particles as well as randomly distributed micropores and occasionally some pore bands inside the powders. These micropores can also be recognized as open pores, which are connected to the particle's surface. The arithmetic mean of the size distribution is MV = 13.06 ± 0.38 μm. Further values of the particle-size distribution are $d_{10} = 2.09$ μm, $d_{50} = 6.51$ μm (mass median diameter) and $d_{90} = 23.17$ μm. The size distribution determined with laser diffractometry coincides well with accompanying SEM examinations. Occasionally, some larger particles > 20 μm can be observed. It is likely that they are formed by means of agglomeration processes.

Dynamic Flowability of the Fine WC-12Co Powder

Figure 3 illustrates the results of the RPA test. The avalanche angle between 33.04 and 78.19° (mean value 53.26°) for the fine powder is relatively high compared to

conventional ones (mean value 35° for the $- 45 + 15$ μm fraction (Ref 37) and increases with rising avalanche energies from 2.06 to 101.62 kJ/kg. Many avalanches are present in the area of high avalanche energies. Higher avalanche angles generally result from a low flowability of the powder and are therefore undesirable. The average avalanche energy is 38.94 kJ/kg. In addition, the avalanche energies also show a broad and bimodal distribution over the number of avalanches, which is generally not considered to be advantageous for the flowability of the powder. The results of the RPA test led to the conclusion that the fine WC-Co powders feature a low flowability. Besides, the highly viscous behavior of the powder could be qualitatively observed during pouring into the powder feeder container. Agglomeration effects were largely prevented by constant heating of the powder before and during thermal spraying.

Process Behavior and Particle Diagnostics

Flame Profile and Chamber Pressure

The flame profile analysis indicates that the increase of the nitrogen flow from NF = 15 L/min to 115 L/min leads to an almost proportional reduction of the flame length (Fig. 4). As demonstrated, the flame length declines continuously from 140 (NF = 15 L/min) to 117 mm (NF = 115 L/min) by a factor of 5 mm per 25 L/min. With the highest nitrogen flow of 115 L/min, a large standard deviation can be observed in the flame length. This is related to two aspects: On the one hand, the flame becomes colder with increasing nitrogen flow. This relationship has also been described by many other researchers and can therefore be regarded as generally accepted (Ref 27, 42-44). Due to lower gas temperatures with higher nitrogen flows, the flame loses its luminosity, which makes it also difficult to determine its length clearly. On the other hand, the larger standard deviation of the flame length at NF = 115 L/min can be attributed to dynamic pulsations of the flame suggesting the presence of process instabilities. Similar results
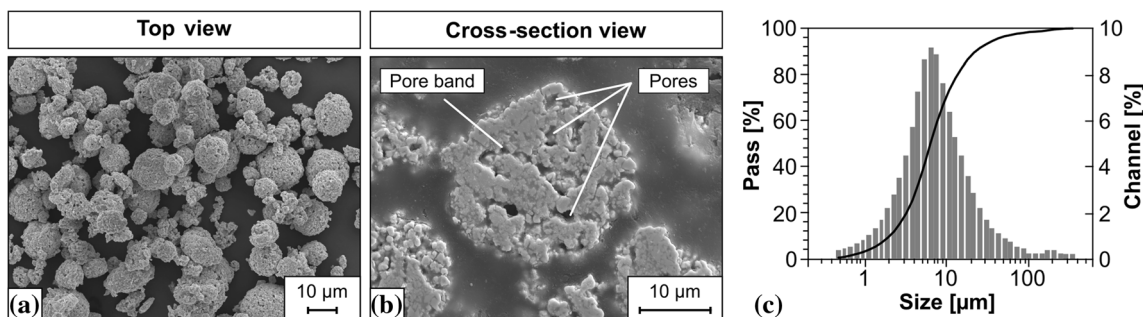

Fig. 2 SEM images of the employed fine WC-12Co powder in (a) top view, (b) cross-sectional view, and (c) volume-based frequency distribution and cumulative size distribution of the agglomerates

Fig. 3 Dynamic flowability of the fine WC-12Co powder analyzed by the RPA test
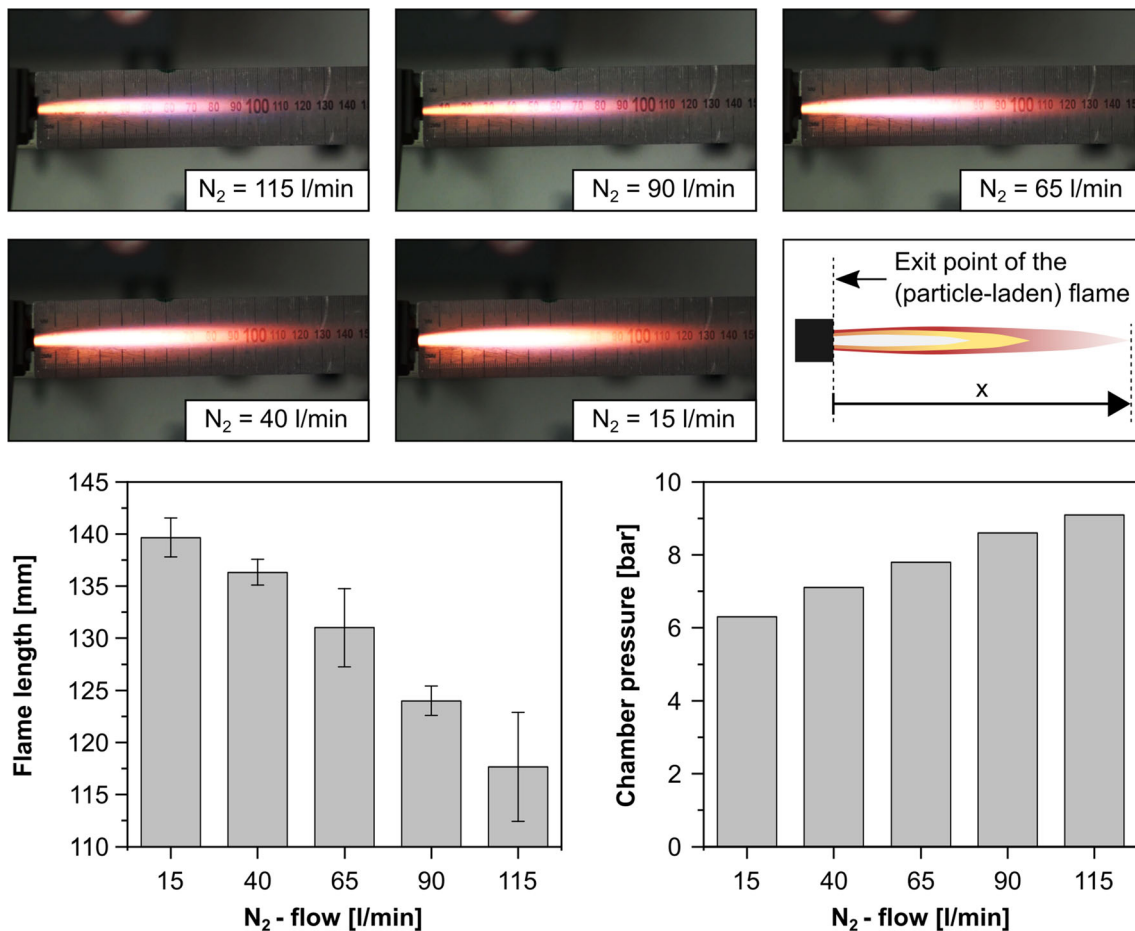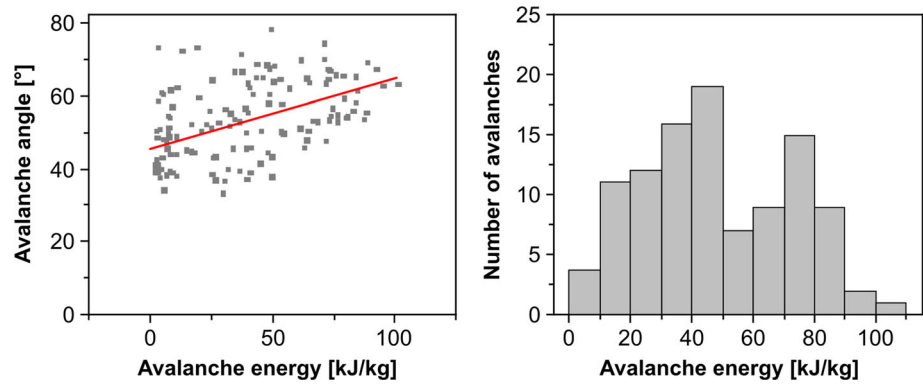

Fig. 4 Influence of varying nitrogen flows on the length and luminosity of the particle jet as well as on the combustion chamber pressure

were found by Tabbara et al. in their study on the computer modeling of titanium particles during warm spraying (Ref 27). The authors reported on fluctuations in both the gas velocity and temperature when the nitrogen flow rate and hence the upstream pressure are increased. They indicate that this effect is brought about by the underexpanded flow regime. The influence of the nitrogen flow on the length and luminosity of the flame is demonstrated in the process images in Fig. 4. As an inert gas, nitrogen does not

participate in the combustion reaction of hydrogen, oxygen and kerosene. The nitrogen flow increases the heat capacity of the combustion gas mixture. The nitrogen is heated during the combustion reaction and thus consumes a part of the thermal energy. As a result, the process gas is cooled down and the spray particles experience less heat transfer when passing through the flame. This results in a shorter and less luminous flame, as shown in the process image at NF = 115 L/min. In contrast, at lower N_2 values, the

combustion gas mixture can relax more slowly as it exits the barrel, resulting in a longer and brighter spray flame. At the same time, the combustion gas mixture has a lower heat capacity, which results in higher particle temperatures.
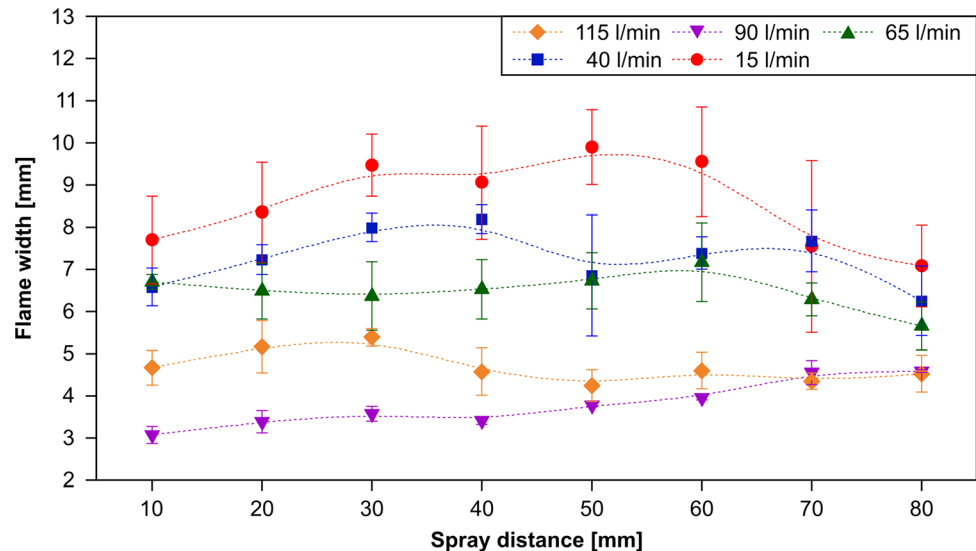
Higher nitrogen flows lead to an increased amount of gas mixture and thus to higher pressures in the combustion chamber (Fig. 4). With an increase of the nitrogen flow from 15 L/min to 115 L/min, the combustion chamber pressure proportionally rises from 6.3 to 9.1 bar by a factor of 0.7 bar per 25 L/min. However, describing the influence of higher chamber pressures on the process gas flow in warm spray processes is complex for the following reasons: If the combustion media (kerosene and hydrogen) and the oxygen flow are unchanged, higher combustion chamber pressures are only achieved by higher nitrogen flows. However, nitrogen does not participate in the combustion reaction, but instead leads to a cooling down of the flame. Besides the larger amount of expanding gas mixtures, the simultaneous effect of the reduced temperature of the process gas flow on the corresponding velocity profile also needs to be considered.

In HVOF processes, the chamber pressure mainly depends on the flow rate of fuel and/or O_2 (Ref 45). Zhao et al. reported that both particle velocity and temperature increase with higher total gas flow rates (Ref 46). In addition, higher total gas flows help to maintain the gas velocity and temperature in the free jet at high levels for a longer distance (Ref 47). Whereas the particle velocity is primarily influenced by the combustion chamber pressure and the expanding gases, the particle temperature is strongly dependent on the fuel/oxygen ratio and the burning enthalpy of the gas (Ref 46, 48). The increased particle velocity is achieved by means of a higher gas density, leading to higher drag forces as well as to an enhanced momentum transfer between the gas phase and particles (Ref 45, 47, 49). Hanson et al. even reports on a linear increase between the chamber pressure and the particle velocity (Ref 50, 51). Totemeier et al. have studied the HVOF spraying of Fe_3Al powders with a JP-5000 HVOF system (Ref 52). In contrast to the decrease in flame length with higher nitrogen flows shown here, the authors observed an opposite effect (i.e., increased flame lengths), but confirmed that increasing chamber pressures lead to higher particle velocities. The authors also concluded that increased flame lengths and higher particle velocities are competing effects, which result in the particle temperature being a complex function of the chamber pressure, the flame temperature and particle residence time in the flame (Ref 52). The increased flame lengths can be explained by the fact that with HVOF spraying, higher chamber pressures are associated with a greater amount of media (kerosene and oxygen) which are burned in the combustion chamber and expanded in the CD nozzle. However, this is

different with warm spray processes, since here (and presented in this study) the higher combustion chamber pressures are achieved only by injecting a higher flow of nitrogen, while the combustible media flow is kept on a constant level. Kuroda et al. simulated the velocity and the temperature of both the gas and the particles for the warm spraying of titanium particles with a size of 30 μm (Ref 17). They reported that increasing the nitrogen flow rate from 500 to 2000 slm resulted in an increase in the pressure in the combustion chamber from 0.5 to 2.0 MPa. However, the gas velocity itself is higher with less nitrogen flow rates due to higher gas temperature (and corresponding larger speed of sound) in the mixing chamber and the barrel. With a higher-temperature gas flow, more heat is transferred to the water-cooled barrel, which results in less decrease in Mach number in the flow direction due to the effect of supersonic Rayleigh flow (Ref 17). They attributed this to the increase in the gas density with the addition of nitrogen, which compensated for the decreased gas velocity. Consequently, the velocity profiles of the titanium particles are almost unaffected by the nitrogen flow rate (Ref 17).

Figure 5 shows the development of the flame width as a function of the spray distance at varying nitrogen flows. The measured flame width values are between 3.07 mm (SD = 10 mm, NF = 90 L/min) and 9.9 mm (SD = 60 mm, NF = 15 L/min). At lower nitrogen flows (NF = 15-40 L/min), larger standard deviations can be observed, which, however, could not be clarified in more detail within the scope of the investigations carried out here. In analogy to the flame length, the average flame width also decreases proportionally with increasing nitrogen flows. This can be attributed to the lower temperature of the process gas and the corresponding existence of fewer hot particles in the fringe area of the flame. An exception is the curve with NF = 90 L/min, which features the smallest flame width, even below the curve with NF = 115 L/min. However, the present results do not allow a satisfactory explanation for this behavior. It is assumed that warm spraying with a nitrogen flow of 90 L/min could provide a good compromise between a sufficient acceleration and heat input into the particles, leading to a homogeneous flame width profile with little spray plume divergence. Regarding the development of the flame width over the spray distance, a slightly different behavior can be observed for higher and lower nitrogen flows. At lower nitrogen flows (NF = 15-40 L/min), the flame expansion is more pronounced than in the medium and high nitrogen flow regions (NF = 65-115 L/min). This behavior is clearly shown in the process pictures in Fig. 4. Furthermore, higher nitrogen flows (NF = 90-115 L/min) generally (regardless of the spray distance) lead to a more homogeneous flame with less scatter of the values for the flame width. However, it should be noted that the variation in the flame width along

Fig. 5 Development of the flame width as a function of the spray distance at varying nitrogen flows

the whole flame axis is only minor and has a maximum difference of 2.5 mm.

Taking the results of this study and the ones from the literature into account, it can be concluded that higher nitrogen flows lead to increasing combustion chamber pressures. At the same time, the gas flow is cooled down, producing a shorter, narrower and less luminous flame. Due to this, the spray particles experience less heat transfer when passing through the flame. However, different results regarding the influence of the nitrogen flow on the process gas velocity and the particle velocity are found in the literature. In the following two sections, the particle temperature and velocity during spraying of fine WC-Co powders with the ID RED gun are therefore presented and discussed.
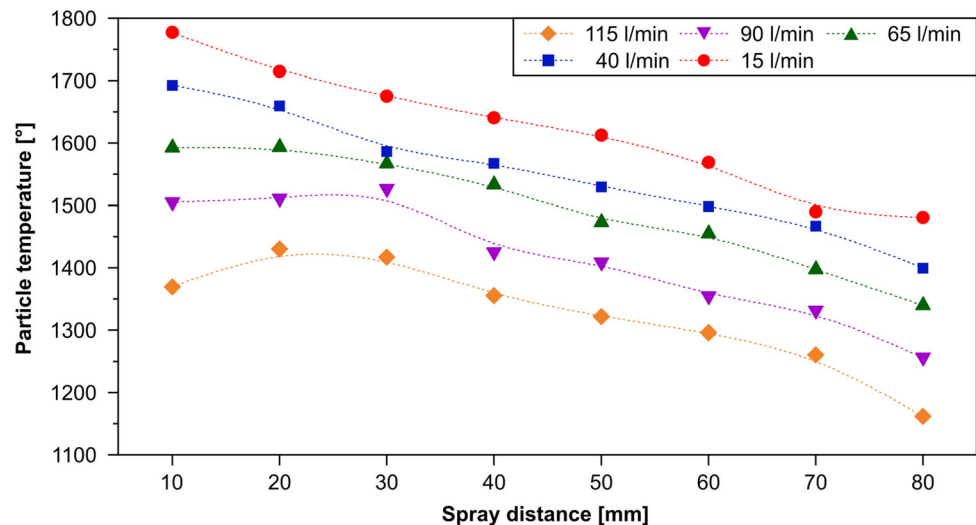
Particle Temperature

The development of the particle temperature in-flight along the spray axis (SD = 10-80 mm) with different nitrogen flows (NF = 15-115 L/min) is demonstrated in Fig. 6. In order to illustrate the particle temperature curves more clearly, the individual points were fitted with the aid of a polynomial model. Warm spraying of fine WC-12Co powders in this study generally showed particle temperatures between a minimum of 1162 °C (SD = 80 mm, NF = 115 L/min) and a maximum of 1777 °C (SD = 10 mm, NF = 15 L/min). For all measurements, highest particle temperatures are generally achieved in the area close to the nozzle exit at SD = 10-30 mm. This behavior was found by many researchers and can be regarded as generally accepted (Ref 20, 27, 29). The temperature profile of the spray particles corresponds to the behavior of the gas temperature after leaving the nozzle, which is highest in the potential core region of the jet, but then rapidly decreases

when mixing with the ambient air, as reported by Kuroda et al. and Molak et al. (Ref 20, 44). In this area, a maximum heat transfer from the flame to the spray particles takes place resulting in maximum particle temperatures.

It is noticeable that with lower nitrogen flows (NF = 15-40 L/min), the particle temperatures are highest at SD = 10 mm, while at medium nitrogen flows (NF = 65) they extend plateau-like over a spray distance between SD = 10 mm and SD = 20 mm. With highest nitrogen flows (NF = 90-115 L/min), the temperature is not highest immediately as the particle jet emerges from the nozzle, but initially rises slightly to their highest values of 1527 °C with SD = 30 mm (NF = 90 L/min) and 1430 °C with SD = 20 mm (NF = 115 L/min), respectively. This behavior can be attributed on the one hand to the rising combustion chamber pressure and the associated increase in particle velocity at higher nitrogen flows. This enlarges and shifts the zone for the heat transfer to the spray particles further downstream into the jet. On the other hand, the explanation of Tabbara et al. in (Ref 27) seems to be plausible here. They reported that nitrogen is not fully mixed with the combustion media by the end of the barrel, even with the injection angled toward the expanding combustion gas (Ref 27). The nitrogen gas travels along the boundary wall and continues to mix along the barrel, essentially producing a nitrogen-rich boundary layer, where the gas temperature and axial velocity are lowered. As a result, the powders, which are injected radially into the supersonic part of the ID gun, experience less heating in the nozzle at higher nitrogen flows and therefore reach their maximum temperature further downstream in the free jet. Besides, it is also likely that the effect of lower gas velocities in the barrel and potential-core region of the jet described by Kuroda et al. (Ref 20), which occurs at higher nitrogen flows due to lower gas temperatures, supports the

Fig. 6 Development of the in-flight particle temperature as a function of the spray distance at varying nitrogen flows. In order to illustrate the particle temperature curves more clearly, the individual points were fitted with the aid of a polynomial model

delayed attainment of highest particle temperatures, since this can lead to a slower heat transfer from the jet to the spray particles.

The further the spray particles move away from the exit point of the barrel (i.e., as the spray distance increases), the more the particle temperatures drop with an almost linear trend for all curves until they reach their lowest values at SD = 80 mm. At this spray distance, the highest particle temperature of 1480 °C is reached for NF = 15 L/min, while NF = 115 L/min produced the lowest particle temperature of 1162 °C. A similar progress of particle temperature was found for ID HVOF spraying of WC-CoCr powders (particle size: − 20 + 3 μm) with spray distances from SD = 30 mm to SD = 70 mm by Gutleber et al. (Ref 53). Whereas highest values are achieved at SD = 30 mm, the velocity continuously decreased with higher spray distances. For the spray distance used for coating trials (50 mm), the particle temperature was measured as 2260 °C. The almost proportional reduction of all particle temperature values with increasing spray distance is mathematically described in a study by Pan et al. (Ref 54) and can be attributed to the gradual decrease in thermal energy of the process gas flow. In a previous study performed by Baumann et al., the in-flight particle behavior of the same fine WC-12Co powder (particle size − 10 + 2 μm) was investigated in a spray distance region from SD = 50 mm to SD = 450 mm using a CJS-HVOF OD gun (Thermico Engineering GmbH, Germany) without nitrogen injection (Ref 55). At the shortest spray distance of SD = 50 mm, significantly higher particle temperatures of 2100 °C were found compared to the results presented here. When the distance was increased to SD = 200 mm, the temperature initially dropped sharply to 1600 °C and finally to 1100 °C with SD = 450 mm (Ref 55).

The comparison of the individual particle temperature curves clearly indicates that the greater the nitrogen flow, the lower the corresponding particle temperature. The increase in the nitrogen flow by 25 L/min leads to an average decrease in the particle temperature of around 100 °C. By increasing the nitrogen flow from NF = 15 L/min to NF = 115 L/min, the temperature could be reduced by a total of about 300 °C.

This proves that increasing nitrogen flows during warm spraying has a demonstrable cooling effect on the process gas flow which is achieved by the heat capacity of nitrogen. In another previous study conducted by Tillmann et al., the development of bond coats for 7YSZ TBCs by means of an IDCoolFlow warm spray process with varying nitrogen flows (NF = 0 L/min, 15 L/min and 100 L/min) and a CoNiCrAlY powder in a fractionation of − 38 + 5.5 μm (Ref 2) was investigated. It was found that the particles sprayed with highest nitrogen flow (NF = 100 L/min) generally showed the lowest particle temperatures in-flight. The values for the particle temperature ranged between 1200 and 1300 °C near the spray gun nozzle exit (SD = 15-30 mm) and decreased to below 1000 °C at the end of the spray plume (SD = 90 mm). These results confirm the findings in the present study. Kuroda et al. simulated the temperature of both the gas and the particles for the warm spraying of titanium particles with a size of 30 μm (Ref 17). They reported that maximum particle temperature can be decreased from 1400 to 900 K by increasing the nitrogen flow rate from 500 to 2000 slm. Watanabe et al. studied the warm spraying of three powder feedstock (Ti, Cu, Al) with different melting temperatures using a modified conventional HVOF equipment (JP5000, Praxair Technology Inc., USA) (Ref 42). According to their research work, jet temperatures and particle temperature decrease both with higher N_2 flow rates and vice versa. In a study by Kim

et al., the temperature of warm sprayed titanium spray particles with a diameter of 30 μm was calculated for nitrogen gas flow rates of KF = 500 and KF = 1500 dm³/min by means of gas dynamics simulations (Ref 56). The authors determined higher particle temperatures about 1250 °C for NF = 500 dm³/min and 850 °C for NF = 1500 dm³/min at the substrate location of 180 mm. This underlines that the nitrogen gas can effectively lower the temperature of in-flight titanium particles.

It can be concluded that with an increase of the nitrogen flow in warm spray processes, the temperature of the process gas and thus of the particles can be effectively reduced. For this reason, warm spray processes generally feature a good suitability for the processing of fine WC-12Co powders. Highest particle temperatures are generally achieved in the area close to the nozzle exit. The further the spray particles move away from the nozzle along the spray jet, the greater the almost linear drop in particle temperature. This is in line with the behavior of the gas temperature after leaving the nozzle. At high nitrogen flows, the heat transfer to the spray particles is shifted further downstream into the jet. As a result, the temperature of the sprayed particles is not highest immediately as the jet emerges from the nozzle, but initially rises slightly to their highest temperatures. Finer spray particles are generally more susceptible to higher temperatures. The temperature of smaller particles in the spray jet rises faster, thus enabling fine particles to achieve a better melting state. However, finer particles lose their temperature faster than larger particles when passing through the flame jet.
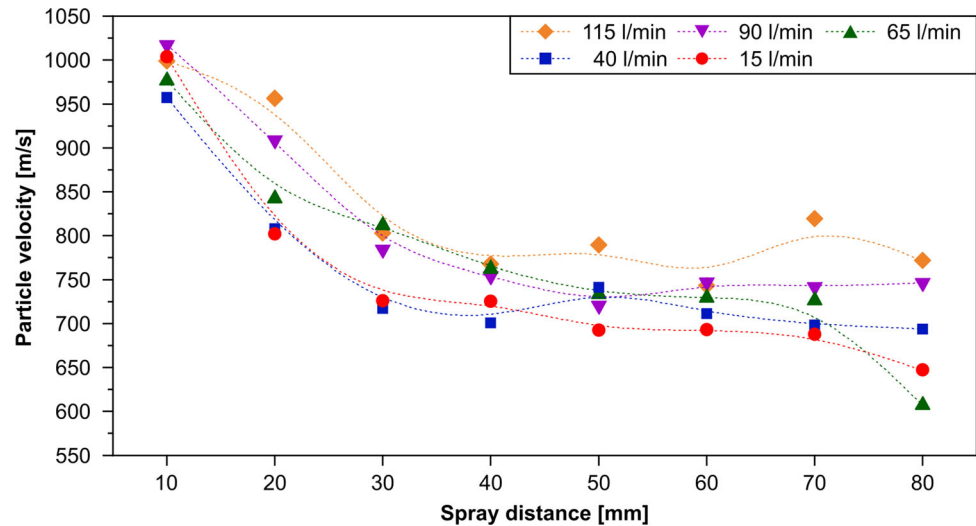
Particle Velocity

Figure 7 illustrates the development of the in-flight particle velocity along the flame axis (SD = 10-80 mm) at varying nitrogen flows (NF = 15-115 L/min). In order to illustrate the particle velocity curves more clearly, the individual points were fitted with the aid of a polynomial model. The particle velocities determined during warm spraying of fine WC-Co powders in this study are between a minimum value of 607 m/s (SD = 80 mm, NF = 65 L/min) and a maximum one of 1017 m/s (SD = 10 mm, NF = 90 L/min). For all nitrogen flows, the particle velocities show an almost similar progress in the spray distance range of SD = 10-60 mm. In all experiments, the particle velocity is highest in the area where the particle jet emerges from the nozzle with SD = 10 mm. This can be attributed to the maximum momentum transfer from the flame to the particles in this area, which decreases with larger distances from the exit point. Similar particle behavior is reported in other studies on HVOF spraying, for instance in (Ref 57-59). Pukasiewicz et al. attributed the higher particle velocities with shorter spray distances to higher drag force

of the process gas flow (Ref 58), which is gradually reduced along the spray plume. Bobzin et al. performed a study on the particle behavior during spraying with an ID CoolFlow HVOF system (Thermico Engineering GmbH, Germany) using WC10Co4Cr as powder feedstock with the fractions − 15 + 5 μm and − 30 + 16 μm (Ref 59). The authors found a gradual decrease in the particle velocity shortly after the particle flow left the nozzle only for the fine powder fraction. With the coarser fraction, the particle velocity remained almost constant along the spray plume. This indicates that the particle size has a large effect on the kinetic behavior in-flight. According to Kuroda et al., highest gas flow velocities are achieved in the area of the nozzle exit (Ref 17). Based on semiempirical equations, they calculated the velocity of the gas jet along the centerline outside the barrel and described its development as follows: The gas velocity initially increases rapidly when it expands through the nozzle. Then, it gradually declines along the length of the barrel due to friction with the inner wall of the barrel. After leaving the barrel, the gas velocity increases stepwise owing to the under-expansion of the jet flow, while it remains constant in the potential core area outside the barrel. When mixing with the ambient air, the gas flow then decreases steadily (Ref 17).

In the free jet at spray distances between SD = 10 mm and SD = 30 mm, a strong and almost linear decrease in the particle velocity from SD = 10 mm to SD = 30 mm (maximum value of 812 m/s with NF = 65 L/min and a minimum value of 718 m/s with NF = 40 L/min) can be detected. During this process, the spray particles lose their largest proportion in kinetic energy. This area of the flame marks the supersonic area of the process gas flow, in which the shock diamonds are formed. Following this area, the curves for the particle velocity gradually flatten at SD = 30-40 mm. Here, the particle velocity drops further, but much less than in the area of shorter spray distances (SD = 10-30 mm). From a spray distance of 40 mm onward to SD = 80 mm, the particle velocities converge almost asymptotically (in a plateau-like region) to an average value between 700 and 775 m/s. With SD = 80, a maximum value of 772 m/s (NF = 115 L/min) and a minimum value of 607 m/s (NF = 65) are achieved. In this area of the flame, the process gas flow has already mixed with the ambient air and noticeably lost its velocity. However, the drag force of the process gas flow keeps the spray particles in this area at an almost constant velocity level. A similar progress of particle velocity was found for ID HVOF spraying of WC-CoCr powders (particle size: − 20 + 3 μm) at spray distances from SD = 30 mm to SD = 70 mm by Gutleber et al. (Ref 53). Whereas highest values are achieved with SD = 30 mm, the velocity continuously decreased with higher spray distances. For the

Fig. 7 Development of the in-flight particle velocity as a function of the spray distance at varying nitrogen flows. In order to illustrate the particle velocity curves more clearly, the individual points were fitted with the aid of a polynomial model

spray distance used for coating trials (50 mm), the particle velocity was measured as 882 m/s.

The curves for the particle velocity at different nitrogen flows shows no significant differences in the range of SD = 30-60 mm. The difference between the absolute values is around 100 m/s. A general examination of the curves shows that the particle velocity with higher nitrogen flows (NF ≥ 65 L/min) consistently reaches higher values than with NF < 65 L/min. Highest particle velocity values are achieved at high nitrogen flows of NF = 115 L/min. This behavior correlates with the increase in the combustion chamber pressure from 6.3 bar (NF = 15 L/min) to 9.1 bar (NF = 115 L/min) at that highest nitrogen flow. During the energy conversion in the de Laval nozzle, the higher pressure of the gas mixture leads to greater expansion of the process gas and consequently to an increase in the particle velocity. Conversely, a nitrogen flow of NF = 15 L/min results in lower particle velocity values due to the minimum combustion chamber pressure of 6.3 bar. According to Hanson and Settles, the particle velocity is primarily affected by combustion pressure and increases almost linearly with it (Ref 50). In turn, the chamber pressure increases at higher total gas flow rates, which is provided by higher nitrogen flows causing an increase in the drag force on the particles (Ref 58). It also has to be noted that increasing the particle velocity leads to a reduction in the dwell time of the particle in the flame and consequently to lower particle temperature (Ref 60).

Between SD = 50 mm and SD = 80 mm, the progress of the particle velocity at highest nitrogen flow of NF = 115 L/min shows a scattering of the values. This is attributed to pulsations of the flame caused by the high nitrogen flow. The sudden drop in particle velocity for NF = 65 L/min with SD = 80 mm is conspicuous. Since this behavior does

not occur in any of the other curves and instabilities within the spraying process were not observed with this parameter, it can be assumed that this is an outlier.

In the previous study by Baumann et al. on the in-flight particle behavior of the same fine WC-12Co powder using a CJS-HVOF OD gun (Thermico Engineering GmbH, Germany) without nitrogen injection, the particle velocity was measured over a spray distance from SD = 50 mm to SD = 450 mm (Ref 55). While with SD = 50 mm the highest particle velocity of 1140 m/s was measured, the particle velocity decreased sharply along the spray plume to 800 m/s at 200 mm and further declines to 500 m/s with SD = 450 mm.

The flow behavior of small particles in the flame generally differs from that of conventional ones. The acceleration of spray particles occurs mainly in the nozzle (Ref 61). Due to their low inertia, fine particles tend to follow the gas flow trajectories (velocity field) much more easily (Ref 34, 62, 63). Dongmo et al. performed comparison of different particle sizes and showed that particulates with sizes less than 20 μm are not able to separate from the gas path (Ref 57). Generally speaking, changes in the spray distance have a stronger influence on small particles than on big ones (Ref 47)

It can be concluded that the nitrogen flow has an influence on the particle velocity. It has been shown that with higher nitrogen flows, the particle velocity consistently reaches higher values than with lower nitrogen flows. Due to the highest gas flow velocities and drag forces in the area where the particle-laden flame emerges from the nozzle, the particle velocity is highest and continuously declines along the spray plume.

Influence of the Spray Distance on the Coating Properties of Planar Samples

Planar steel specimens were coated according to the parameters given in Table 1 while varying the spray distance using the OFAT method and then characterized. Cross-sectional analyses indicate a homogeneous and macro-defect-free microstructure at spray distances from 30 to 50 mm (Fig. 8, 9e, f and g). At spray distances below 30 mm, metallographic investigations reveal the presence of macroscopic defects (Fig. 9a, b, c and d). At 20 mm, these defects occur much less frequently and rather sporadically, suggesting that the coating structure is almost intact. At a spray distance of 10 mm, the coating structure is predominantly interspersed by angular growth defects and micro-/macro-cracks. These defects emerge from the surface as macroscopic protuberances and are occasionally surrounded by cavities and cracks. They appear as regular patterns with a preferred orientation and sizes of a few hundred micrometers as well as different distances between them. As shown in Fig. 9a, b, c and d, three major types of defects can be found and differentiated in this study:

- *Micro- and macro-cracks in the coating structure*: This type of defect can only be identified at the shortest spray distance SD = 10 mm. They are mainly present as horizontal cracks in the subsurface area of the coating (Fig. 9d). In some cases, these cracks propagated angularly through the coating structure to the substrate. Reasons for these cracks are mainly thermal stress and insufficient intersplat connections. While the former is caused by the intense heat transfer from the flame to the surface, the latter results from the low degree of melting of the particles due to the short dwell time when passing through flame.
- *Insufficiently melted spray particle clusters:* These defects are almost spherical or lenticular and can only be found on the immediate surface of the coating

(Fig. 9a). Occasionally, these defects are surrounded by cracks or pores. This type of defect is mainly observed at SD = 10 mm. They are obviously formed by an insufficient acceleration and melting of the particles at short spray distances resulting in a poor plastic deformation behavior when they impact on the substrate.

- *Angular growth defect structures within the coating:* Such defects occur in different sizes and at different angles (Fig. 9b, c). They also expand to different depths into the coating structure; in some cases, they also reach the substrate. Sometimes, two of such structures are closely connected or even superimposed. It is conspicuous that these defects show a layered structure. It can therefore be assumed that they are formed at a certain point of time during coating and then grow successively. Consequently, they do not belong to the second defect category. In some cases, the individual layers are delaminated from each another. It is likely that this is due to thermal stress formation. Macroscopic cracks, pore bands, and thin oxygen-rich zones can be identified between larger voids (sometimes filled with impurities). However, the formation mechanism of these growth defects is much more complex since no correlation was found to other imperfections in the coating structure or at the interface between the coating and the substrate (e.g., roughness peaks that lead to shadowing effects).

It is noticeable that all the defects mentioned are not visible at the edge areas of the coated planar samples. This suggests that flow effects of the particles in the flame jet could be mainly responsible for their formation. The bow-shock effect of the process gas flow may have a substantial influence here (Ref 2, 64). Similar findings were reported by Gutleber et al. (Ref 53), who studied the coating deposition at short spray distances by using a novel ID HVOF spray gun (DiamondJet Vortex DJV ID, Oerlikon
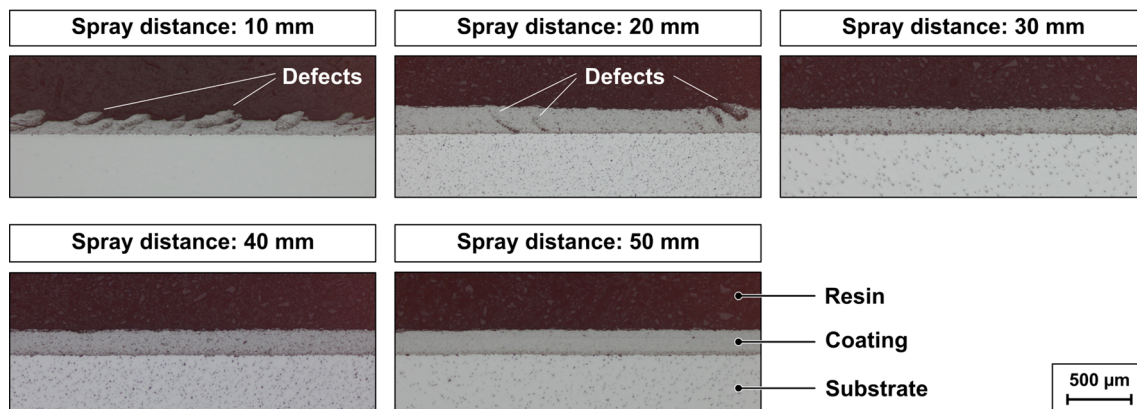

Fig. 8 Coating structures on the planar steel samples at different spray distances
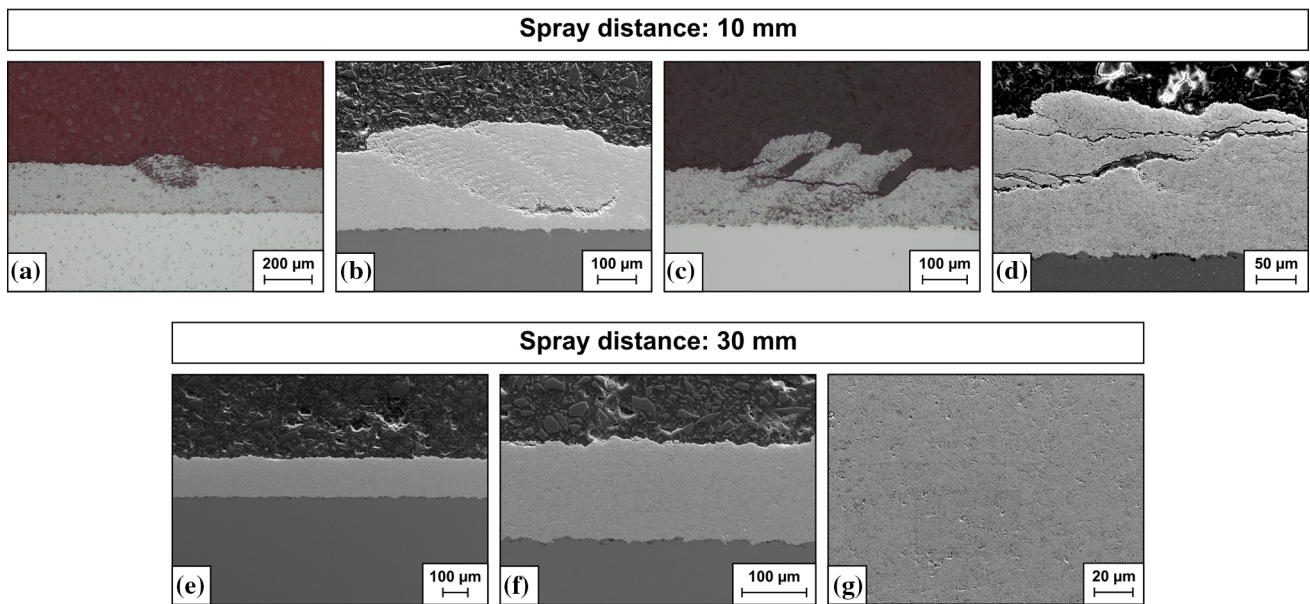
Fig. 9 Coating defects at spray distances of 10 mm: (a) insufficiently melted spray particle clusters, (b, c) angular growth defect structures within the coating, (d) micro- and macro-cracks in the coating structure as well as (e, f, g) homogenous and macro-defect-free coating structure at a spray distance of 30 mm
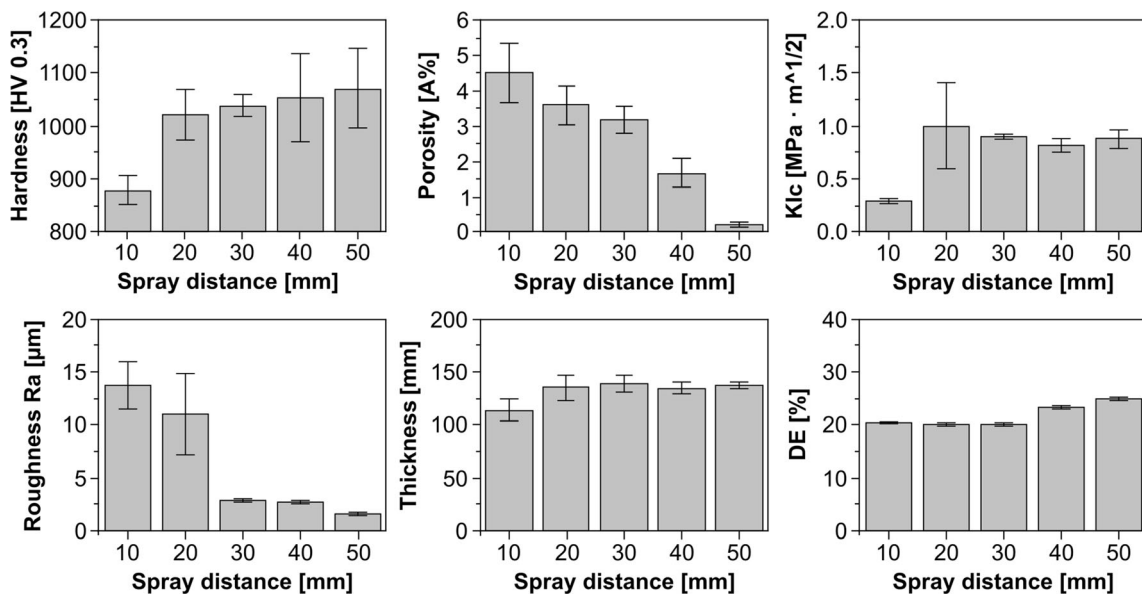

Fig. 10 Coating properties and deposition efficiency (DE) depending on the spray distance during coating of the planar steel samples

Metco, Switzerland). The authors reported that due to the turbulent flow near the substrate surface, the fine particles could have reached the fringe areas of the process gas jet, which in turn lead to a deceleration and cooling of the particles.

Image analyses verify that the increase in the spray distance leads to an almost proportional decrease in the porosity. Thus, the porosity drops slightly from 4.51 ± 0.83 % at SD = 10 mm to 3.18 ± 0.37 % at SD = 30 mm (Fig. 10). At a spray distance of 40 mm, the porosity halves to 1.67 ± 0.4% and drops again by a factor of 7 to 0.23 ± 0.08 % at SD = 50 mm. For short spray distances in the range of 10 to 30 mm, it is conspicuous that the porosity is comparatively high for a finely structured WC-12Co coating. This is due to the reduced dwell time for the heat and momentum transfer at short spray distances. Hence, the particles achieve only a low melting degree and a weaker deformation ability when they hit the substrate surface. In addition, the porosity is superimposed

by the growth defects in the coating which themselves feature a higher porosity.

In analogy to the development of the porosity, a decline in surface roughness can be observed with increasing spray distances (Fig. 10). A high mean roughness Ra of 13.69 ± 2.22 μm is measured at SD = 10 mm, which decreases to Ra = 11.08 ± 3.83 μm at SD = 20 mm. With growing spray distances up to 30 mm, the mean roughness Ra distinctly drops to 2.93 ± 0.13 μm, respectively, to 2.72 ± 0.24 μm at SD = 40 mm. With SD = 50 mm, the mean roughness Ra finally decreases to 1.65 ± 0.12 μm. In accordance with the porosity measurement, the increased surface roughness for short spray distances below 30 mm can be ascribed to the coating imperfections (i.e., growth defects of the coating) which lead to protruding asperities. During coating of the planar samples, a sporadic "spitting" of fine powders from the ID spray gun was observed. This occurred in the form of a sudden and rapid (dust cloud-like) ejection of a large amount of powder material. It is very likely that this effect is due to a temporary clogging of the powder injectors (or hoses) caused by a sudden formation of agglomerations that were occasionally blown off by the carrier gas flow. Since this effect only appeared rarely and had no negative impact on the coating quality or the surface topography, it was not considered relevant during coating of the flat samples. As opposed to that, from SD = 30 mm, the reduction in the surface roughness can be attributed to a more intense heat transfer to the spray particles due to an increased dwell time, which leads to an improved flattening behavior during impact.

As proven by gravimetrical measurements, the deposition efficiency at SD = 10-30 mm is almost constant and amounts to 20.23 ± 0.17 %. With SD > 30 mm, the deposition efficiency slightly increases to 23.50 ± 0.18 % at SD = 40 mm as well as to 24.94 ± 0.18 % at SD = 50 mm. The spray experiments conducted in this study generally show significantly lower deposition efficiencies at all spray distances than those achieved with a traditional (OD) HVOF spray process using the same WC-12Co powder feedstock. The latter ranges between 27.4 and 61.7 % and features a value of 35 ± 0.25 % for the optimized coatings (Ref 65). It can be assumed that the low deposition efficiencies are caused by the lower combustion power and the more compact design of the ID RED gun in contrast to traditional spray guns. As a result, the fine powders achieve a lower degree of melting and thus increasingly bounce off the surface.

Figure 11 illustrates the phase evolution of the powder feedstock and the ID coatings sprayed on planar steel samples in the 2θ angular range from 30° to 50° detected by means of XRD. As shown, the HVOF sprayed WC-Co coatings are mainly composed of WC as well as traces of WC_{1-x}- or $M_{12}C$-type carbides such as Co_6W_6C. In this

respect, the strongest line at $2\theta = 42.89°$ (corresponding to the (200) reflection for WC_{1-x}, space group: Fm3m (225) is close to the position of the strongest line ($2\theta = 43.08°$ for the (511) reflection) of Co_6W_6C (space group: Fd3m (227), which ultimately does not allow a precise differentiation. A distinct reflection of cubic Co, as observed for the feedstock, cannot be clearly detected in the WC-Co coatings. However, the XRD patterns of the WC-Co coatings suggest the presence of amorphous or partially crystalline Co. Moreover, the XRD patterns also indicate the absence of elementary W, W_2C and Co_3W_3C within the experimental resolution. When comparing the XRD patterns of the different WC-Co coatings (i.e., in dependency of the spray distance), only minor differences in phase composition can be observed. Accordingly, it is found that with increasing spray distance, the formation of WC_{1-x} and Co_6W_6C is more pronounced. Simultaneously, only a small proportion of crystalline Co is present suggesting the occurrence of amorphous or partially crystalline Co being more likely. As opposed to that, for a reduced spray distance (i.e., SD < 30 mm), only some minor contents of Co_6W_6C and WC_{1-x} can be found in the WC-Co coatings. In general, WC decomposition phenomena in HVOF sprayed WC-Co coatings are primarily caused by partial overheating of WC particles. The decarburization emerges from the thermal decomposition of WC to W_2C and W. However, in the present study neither W nor W_2C can be found within the experimental resolution. The decomposition of the stoichiometric hexagonal WC is initiated at temperatures above 3058 K to L+ C (L = liquid), whereas, when exposed to oxygen, the decomposition begins at approximately 823 K (Ref 66). The non-stoichiometric WC_{1-x} with a cubic structure is only stable above 2798 K. Below this temperature (i.e., down to room temperature), its formation can only be preserved by supercooling. Regarding the overheating of spray particles, Li et al. (Ref 67) claimed that a part of WC dissolves into the Co matrix (i.e., carbon diffuses into the Co matrix). Opposed to this, Zhan et al. (Ref 68) reported that Co may also diffuse into WC. The authors concluded that the decomposition of WC promotes the formation of M_6C-type carbides (e.g., Co_3W_3C) and $M_{12}C$-type carbides (e.g., Co_6W_6C). Suetin et al. (Ref 69) and Li et al. (Ref 70) examined the ground-state properties of ternary compounds from the Co-W-C system such as the M_6C-type and $M_{12}C$-type carbides. They clarified that among the investigated eta carbides Co_6W_6C is the most thermodynamically stable form, which corresponds to the findings obtained from the XRD analysis in the present study. With respect to the absence of a distinct reflection of a crystalline Co phase, it can be stated that the rapid solidification of the Co-binder phase when splashing onto the substrate prevents a crystallization so that a predominantly amorphous Co phase is formed. This phenomenon has already been

Fig. 11 Phase evolution of the powder feedstock and the ID coatings sprayed on planar steel samples in the 2θ angular range from 30° to 50° detected by means of XRD
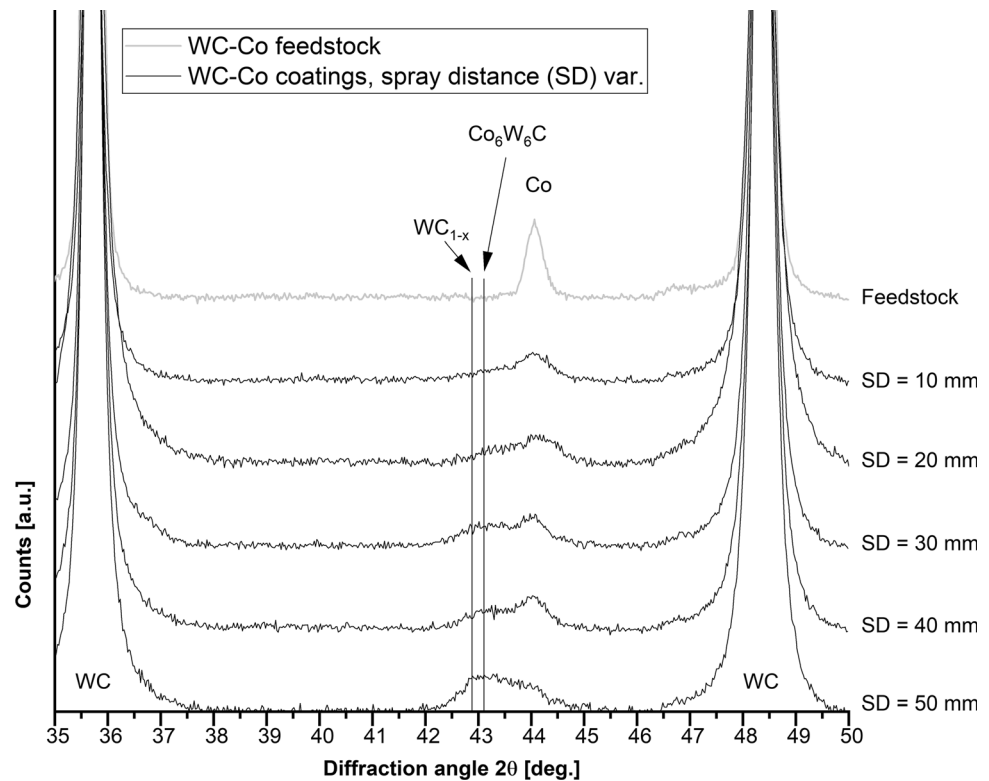
observed in conventional HVOF sprayed WC-Co coatings derived from nanostructured WC-Co feedstock (Ref 71).

In terms of the microhardness, it can be observed that the successive reduction in the spray distance from 50 to 20 mm is initially accompanied by a slight decrease from 1070 ± 75 HV 0.3 to 1021 ± 48 HV 0.3. At the shortest spray distance of 10 mm, Vickers indentation tests reveal a noticeable drop in microhardness to 879 ± 26 HV 0.3. It is conspicuous that the microhardness obtained from the WC-Co coatings is comparatively low. As previously demonstrated by the authors in (Ref 72), a microhardness greater than 1200 HV0.3 was achieved for a conventional HVOF-sprayed WC-Co coating derived from the same powder feedstock used within this study. It can be assumed that higher contents of Co_6W_6C correspond to decreasing amounts of WC resulting in a reduced microhardness.

With respect to the fracture toughness, the lowest value of K_{IC} of 0.30 ± 0.02 MPa $\cdot$ m$^{1/2}$ was measured for coatings sprayed at SD = 10 mm. The fracture toughness K_{IC} of all other coatings (i.e., at spray distances of 20 to 50 mm) is higher and amounts to an average value of 0.87 ± 0.06 MPa $\cdot$ m$^{1/2}$. It is striking that the fracture toughness K_{IC} is remarkable low compared to those reported for WC-Co-cemented carbides (Ref 73) or conventional HVOF-sprayed WC-Co coatings (Ref 74-76). Chivavibul et al. (Ref 75) evaluated that the degree of decarburization of HVOF-sprayed WC-Co coatings represents a distinct influencing factor on the fracture toughness

K_{IC}. The authors clarified that the fracture toughness K_{IC} decreased with higher carbon loss, suggesting that the low fracture toughness K_{IC} within this study can be attributed to extensive decarburization. As reported by Li et al. (Ref 70), the ratio of bulk modulus to shear modulus is frequently used to indicate the ductility of ternary compounds, thus substantiating the fact that Co_6W_6C is less ductile. In this respect, the absence of crystalline Co also contributes to a reduced fracture toughness K_{IC}. However, it is suggested that the low microhardness for a spray distance of 10 mm can be attributed to coating defects described above.

Pulsford et al. investigated the ID coating of a WC-10Co-4Cr powder feedstock with particle size fraction of $-15 + 5$ µm (Ref 32). A microhardness of 1201 ± 106 HV 0.3 and a fracture toughness of 3.92 ± 0.36 MPa $\cdot$ m$^{1/2}$ were measured. These results are significantly better than the ones achieved in this study. In another study by these authors (Ref 32), it is reported that due to the lower spray distance, the coatings achieve higher porosity and thus lower density. In addition, the dissipation of heat may be reduced when coating an internal surface, meaning that substrate temperatures will increase, further resulting in a greater oxidation of the splats post-impact.

In the previous study on the OD coating by Baumann et al. using a CJS-HVOF gun (Thermico Engineering GmbH, Germany), the same fine WC-12Co powder $(-10 + 2$ µm) was sprayed with optimized parameter settings and the corresponding finely structured coatings

were analyzed. At SD = 170 mm, a deposition efficiency of 35 ± 0.25 %, a fracture toughness K_{IC} of 2.44 ± 0.39 MPa · m$^{1/2}$, a microhardness of 1340 ± 30 HV 0.3, a porosity of 1.03 ± 0.06 % and a roughness of Ra = 1.75 ± 0.03 μm were achieved. The comparison of the results shows that the OD coatings generally achieve a better performance regarding microhardness, porosity, fracture toughness and roughness Ra than the ID coatings presented in this study, which were produced with lower combustion power of the gun and significantly shorter spray distances. In addition, a better deposition efficiency is achieved with the OD gun. Whereas the microstructure of the OD coatings appears nearly dense and homogeneous and the surface macroscopically almost smooth, the ID coatings produced at short spray distances < 30 mm feature various defects and an increased surface roughness. However, at largest spray distances of SD = 50 mm, the ID coatings also achieve good (or even better) properties than the optimized OD coatings regarding the roughness value Ra = 1.65 ± 0.12 μm and the porosity of 0.23 ± 0.08 %. The hardness and toughness of the ID coatings values are in turn significantly lower with all spray distances compared to the OD coatings. While the ID coatings achieve an average microhardness which is 20 % (SD = 50 mm) to 34 % (SD = 10 mm) lower than the OD coatings, the fracture toughness was also lower by an average of 64 % (SD = 50 mm) and 86 % (SD = 10 mm). Due to these significantly worse properties (especially in terms of microhardness and toughness), it is expected that the ID coatings will achieve a substantially lower wear performance. Therefore, the ID spray process/the ID coatings needs to be further analyzed and optimized in future studies.

Transfer of the Results to ID Coating of Steel Tubes

The steel tubes were coated using a spray distance of 20 mm. This short spray distance was chosen for several reasons. Due to the small inner tube diameter of 81.6 mm, spray distances larger than 30 mm were generally not feasible. In order to explore the possibilities and limits of ID coating at very short spray distances, it was therefore advisable to use the shortest possible spray distance, i.e., SD = 20 mm in this case. On the other hand, the differences in the coating properties previously applied to the planar specimens at SD = 20 mm and SD = 30 mm were only minor. However, spraying with a shorter distance of 10 mm was not performed for different reasons: the severe coating defects, the intense heat transfers to the surface and the risk of a collision with the tube wall due to a marginal imbalance in component rotation, which could lead to damages of the ID gun. Since the uncooled internal coating generally led to a strong heating and glowing of the tubes,

an internal air-cooling system (mounted on the ID gun) and an external one had to be applied.

The coating results examined at various positions on the tube inner surface (with greater or lesser extent of draw marks and unevenness) are demonstrated in Fig. 12. As shown, the ID coating of tubes with a short spray distance of SD = 20 mm successfully leads to a deposition and adhesion of the spray particles on the inner tube surface and finally to a coating development with the following average values (strongly defective areas excluded): a porosity of 0.45 ± 0.14 %, a layer thickness of 157 ± 20 μm, a roughness of Ra = 6.42 ± 0.95 μm and a microhardness of 950 ± 72 HV 0.3. These coating properties are comparable to those previously applied to planar specimens and confirms that a transfer of the results to the tubes could be successfully realized. However, comparing these results with these provided in the study by Baumann et al. regarding the development of finely structured OD coatings using the same fine WC-Co powder (− 10 + 2 μm), it is noticeable that the ID coatings by far do not reach the properties of the OD coatings (Ref 55). This mainly results from the lower combustion power of the employed ID RED spray gun and the corresponding shorter spray distances necessary for the ID coating. Due to this, the spray particles experience a less sufficient melting state and deformation ability when impacting on the substrate surface. Consequently, the coatings have a much more porous structure with a weaker bond between the individual splats. Furthermore, coatings defects arise, which additionally decreases the coating strength.

In terms of the coating results, three characteristic zones on the tube inner surface can be distinguished. In the first zone (position 1), the coatings have an almost homogeneous and macro-defect-free structure (position 1 in Fig. 12a). Separated individual layers can rarely be observed. Also, a layered defect structure can be found at position 2, between which seams of pores and oxides as well as cracks have formed. The individual layers have partially separated from each other to a greater or lesser extent. It is noticeable that this defect structure is mainly found in areas where fine powder agglomerates have been formed in the flame due to "spitting" effects and deposited on the tube walls, which at the same time also represent process instabilities. These deposited powder agglomerates can be clearly observed at position 2 in Fig. 12a. It can be assumed that a local overheating of powder particles has occurred here, which have formed due to the agglomeration of particularly fine, matrix-rich particles during the feeding or spray process. Likewise, the pore bands could have resulted from a partial drift of fine powders into the jet fringes. While the powders in the center of the jet melt strongly and possibly overheat, the drifted particles only experience an insufficient heating. Poor interconnections
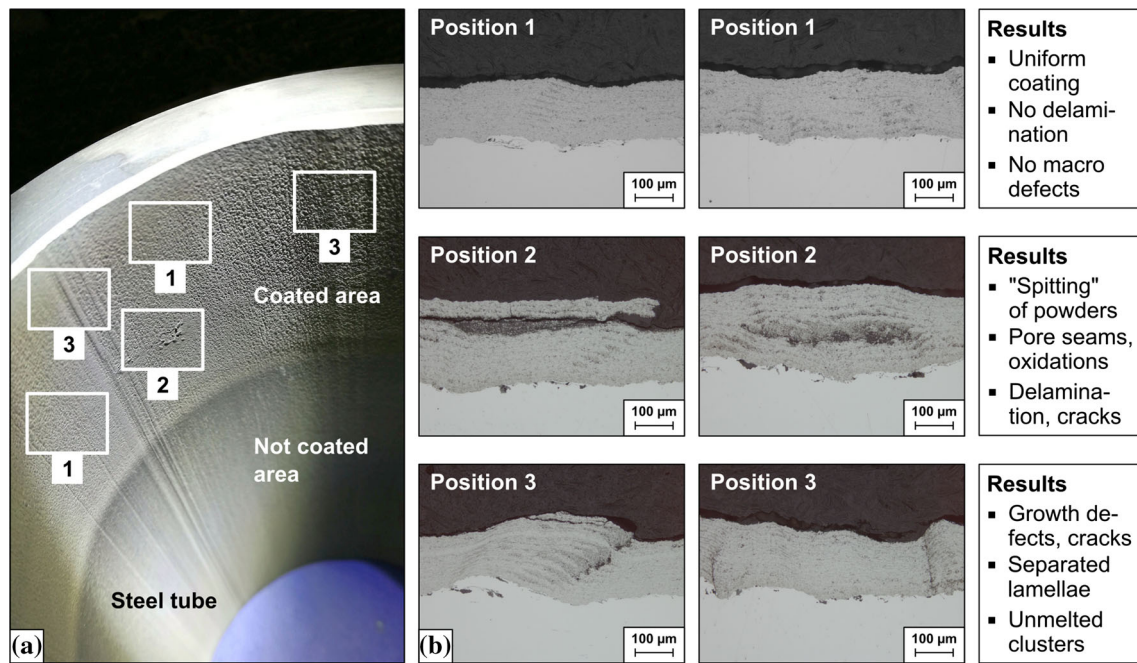
Fig. 12 Results of the coating of steel tubes at a spray distance of 20 mm examined at various positions on the inner surface: (a) photographs of the inner tube surface taken by camera, (b) cross-sectional images of the coating and the interface between coating and the steel tube

between the splats and thermal stresses may then have promoted a detachment of the individual layer lamellae and formed the crack in between. The exact origin of this defect structure could not be fully elucidated in this study. Consequently, further future investigations are required here. The "spitting" of powder agglomerates has not been regarded as majorly relevant during coating of the planar samples. In contrast, for the ID coating of tubes the effect becomes significantly more apparent, since heat, unmelted powder particles and exhaust gases cannot easily leave the coating zone and thus affects the microstructure more intensely. The third zone (position 3) shows growth defect structures and unmelted particle clusters similar to the coating of the planar samples (position 3 in Fig. 12a). However, the latter only occurs rarely. The growth defect structure is characterized by individual lamellae, which are clearly separated from each another. It can be noticed that such growth defects are often formed (or even grown) on drawing marks and irregularities on the inner tube surface. Compared to the coating of planar samples, it can also be assumed that flow effects are the main reason for these defects. In addition, these defects are often accompanied by vertical or angular macro cracks. Sometimes these cracks propagate through the coating structure to the substrate. Obviously, the delamination and cracks are formed by shadowing effects of the process gas flow and the formation of thermal stress during coating. It is expected that these imperfections will cause the coating to fail quickly in wear application. To reduce this effect, it seems advisable to reduce the unevenness of the inner surface of the tubes by means of an appropriate pre-treatment before grit-blasting and applying the finely structured WC-12Co coatings. However, negative effects on the coating adhesion should be expected.

Conclusion

The results in this study show that warm spraying of fine WC-12Co powders (− 10 + 2 μm) with higher nitrogen flows (NF = 90-115 L/min) leads to increased chamber pressures and higher particle velocities. However, the particle velocity decreases sharply along the spray plume shortly after the particle jet exits the nozzle. At the same time, lower particle temperatures are achieved at higher nitrogen flows, which could be reduced by about 300 °C overall. In this course, the flame plume is shorter, narrower and less luminous. The risk of an overheating of the spray particles and the substrate can be further reduced in this way. Warm spray processes therefore generally feature a good suitability for the processing of fine powders. However, nitrogen flows ≥ 115 L/min should be rather prevented as they can cause pulsations and instabilities of the flame.

The spray distance has a great effect on the microstructure and the coating properties such as the microhardness, fracture toughness, porosity and roughness. In contrast, the deposition efficiency and the coating

thickness are only marginally influenced by altering the spray distance. Only low deposition efficiencies of 20 to 25 % have been achieved for the production of ID coatings. It was found that with increasing spray distances (i.e., SD > 30 mm), the formation of WC_{1-x} and Co_6W_6C is more pronounced. However, other undesired phases like W or W_2C could not be detected in the coatings.

The produced finely structured WC-12Co ID coatings in this study do not achieve the same properties as OD coatings. While the microhardness and the fracture toughness of the ID coatings show lower values than the OD ones, their porosity and roughness are higher. The shortest feasible spray distance, which leads to coatings with only moderate defects in the microstructure, was SD = 20 mm. Planar steel samples as well as steel tubes with an internal diameter of 81.6 mm could be successfully coated at this spray distance. However, the microhardness and the fracture toughness are relatively low and thus need to be optimized in further investigations. With a spray distance of 30 mm, the coating structure is more homogeneous and nearly free of any macro-defects. In contrast, severe defects occur at a spray distance of 10 mm, which reduce the cohesive strength and therefore have a negative effect on microhardness, toughness and porosity. In addition, the defects protruding from the surface lead to high roughness values.

Three major types of defects could be observed after spraying with short spray distances, particularly at 10 mm: cracks, insufficiently melted spray particle clusters and angular growth defect structures. It is very likely that they are caused by two effects: (1) an insufficient melting and acceleration of the spray particles caused by short dwell times, (2) flow effects caused most likely by flow deflection near the surface, for instance the bow-shock effect. However, the formation mechanisms of these defects need to be investigated and clarified in further studies.

The ID coatings sprayed on the planar steel samples and on steel tubes at SD = 20 mm feature similar properties and coatings defects. Therefore, the transfer of the coating results to tubes seems to be possible. However, in contrast to the planar samples, the coating of tubes imposes more complex conditions, since the heat, the exhaust gases and the rebounded material cannot easily leave the coating zone. It is expected that specially optimized powders (for instance by plasma spheroidizing) with higher matrix content can reduce the defects and improves the coating properties.

References

1. P. Ernst, SUMEBore—The Coating Solution to Protect Cylinder Liner Surfaces, *SAE Int. J. Eng.*, 2012, **5**, p 1802–1811.

2. W. Tillmann, C. Schaak, L. Hagen, G. Mauer and G. Matthäus, Internal Diameter Coating Processes for Bond Coat (HVOF) and Thermal Barrier Coating (APS) Systems, *J. Therm. Spray Technol.*, 2019, **28**(1), p 233–241.

3. Mahle GmbH, "Zylinderkomponenten: Eigenschaften, Anwendungen, Werkstoffe," 2nd ed., Springer Vieweg, 2015, https://doi.org/10.1007/978-3-658-09546-8.

4. A. Milanti, V. Matikainen, G. Bolelli, H. Koivuluoto, L. Lusvarghi and P. Vuoristo, Microstructure and Sliding Wear Behavior of Fe-Based Coatings Manufactured with HVOF and HVAF Thermal Spray Processes, *J. Therm. Spray Technol.*, 2016, **25**(5), p 1040–1055.

5. B. Gries, "HVAF – Chancen und Herausforderungen für Anwender und Pulverproduzenten (HVAF – Chance and Challenge for Users and for Powder Producers)," *11. Kolloquium Hochgeschwindigkeits-Flammspritzen/HVOF Spraying 2018*, (Erding (Germany)), 2018, p 93–100. https://www.gts-ev.de/hvof/download/HVOF-Proc_2018.cont.pdf.

6. M. Jadidi, S. Moghtadernejad and A. Dolatabadi, A Comprehensive Review on Fluid Dynamics and Transport of Suspension/Liquid Droplets and Particles in High-Velocity Oxygen-Fuel (HVOF) Thermal Spray, *Coatings*, 2015, **5**(4), p 576–645.

7. S. Kamnis and S. Gu, 3-D Modelling of Kerosene-Fuelled HVOF Thermal Spray Gun, *Chem. Eng. Sci.*, 2006, **61**(16), p 5427–5439.

8. L.-M. Berger, "Hartmetallschichten—Historie und Perspektiven (Hardmetal Coatings—History and Perspective)," *11. Kolloquium Hochgeschwindigkeits-Flammspritzen/HVOF Spraying 2018*, (Erding (Germany)), 2018, p 57–72. http://publica.fraunhofer.de/documents/N-515839.html.

9. D. Zhang, S.J. Harris and D.G. McCartney, Microstructure Formation and Corrosion Behaviour in HVOF-Sprayed Inconel 625 Coatings, *Mater. Sci. Eng. A*, 2003, **344**(1–2), p 45–56.

10. L. Jacobs, M.M. Hyland and M. De Bonte, Comparative Study of WC-Cermet Coatings Sprayed via the HVOF and the HVAF Process, *J. Therm. Spray Technol.*, 1998, **7**(2), p 213–218.

11. F. Tarasi, M.S. Mahdipoor, A. Dolatabadi, M. Medraj and C. Moreau, HVOF and HVAF Coatings of Agglomerated Tungsten

Carbide-Cobalt Powders for Water Droplet Erosion Application, *J. Therm. Spray Technol.*, 2016, **25**(8), p 1711–1723.

12. D. Tejero-Martin, M. Rezvani Rad, A. McDonald, and T. Hussain, Beyond Traditional Coatings: A Review on Thermal-Sprayed Functional and Smart Coatings, *J. Therm. Spray Technol.*, 2019, **28**(4), p 598–644.

13. H. Katanoda, T. Kiriaki, T. Tachibanaki, J. Kawakita, S. Kuroda and M. Fukuhara, Mathematical Modeling and Experimental Validation of the Warm Spray (Two-Stage HVOF) Process, *J. Therm. Spray Technol.*, 2009, **18**(3), p 401–410.

14. V. Matikainen, G. Bolelli, H. Koivuluoto, M. Honkanen, M. Vippola, L. Lusvarghi and P. Vuoristo, A Study of Cr3C2-Based HVOF- and HVAF-Sprayed Coatings: Microstructure and Carbide Retention, *J. Therm. Spray Technol.*, 2017, **26**, p 1239–1256.

15. R.K. Kumar, M. Kamaraj, S. Seetharamu, T. Pramod and P. Sampathkumaran, Effect of Spray Particle Velocity on Cavitation Erosion Resistance Characteristics of HVOF and HVAF Processed 86WC-10Co4Cr Hydro Turbine Coatings, *J. Therm. Spray Technol.*, 2016, **25**(6), p 1217–1230.

16. Q. Wang, S. Zhang, Y. Cheng, J. Xiang, X. Zhao and G. Yang, Wear and Corrosion Performance of WC-10Co4Cr Coatings Deposited by Different HVOF and HVAF Spraying Processes, *Surf. Coat. Technol.*, 2013, **218**, p 127–136.

17. S. Kuroda, M. Watanabe, K. Kim and H. Katanoda, Current Status and Future Prospects of Warm Spray Technology, *J. Therm. Spray Technol.*, 2011, **20**, p 653–676.

18. J. Kawakita, S. Kuroda, S. Krebs and H. Katanoda, In-Situ Densification of Ti Coatings by the Warm Spray (Two-Stage HVOF) Process, *Mater. Trans.*, 2006, **47**(7), p 1631–1637.

19. J. Kawakita, S. Kuroda, T. Fukushima, H. Katanoda, K. Matsuo and H. Fukanuma, Dense Titanium Coatings by Modified HVOF Spraying, *Surf. Coat. Technol.*, 2006, **201**(3–4), p 1250–1255.

20. S. Kuroda, J. Kawakita, M. Watanabe, and H. Katanoda, Warm Spraying—A Novel Coating Process Based on High-Velocity Impact of Solid Particles, *Sci. Technol. Adv. Mater.*, 2008, **9**(3), p 033002.

21. M. Watanabe, C. Pornthep, S. Kuroda, J. Kawakita, J. Kitamura and K. Sato, Development of WC-Co Coatings by Warm Spray Deposition for Resource Savings of Tungsten, *J. Jpn. Inst. Met.*, 2007, **71**(10), p 853–859.

22. M. Watanabe, M. Komatsu and S. Kuroda, WC-Co/Al Multilayer Coatings by Warm Spray Deposition, *J. Therm. Spray Technol.*, 2012, **21**(3–4), p 597–608.

23. H. Wang, Q. Qiu, M. Gee, C. Hou, X. Liu and X. Song, Wear Resistance Enhancement of HVOF-Sprayed WC-Co Coating by Complete Densification of Starting Powder, *Mater. Des.*, 2020, **191**, p 108586.

24. P. Chivavibul, M. Watanabe, S. Kuroda, J. Kawakita, M. Komatsu, K. Sato and J. Kitamura, Development of WC-Co Coatings Deposited by Warm Spray Process, *J. Therm. Spray Technol.*, 2008, **17**(5–6), p 750–756.

25. J. Kawakita, H. Katanoda, M. Watanabe, K. Yokoyama and S. Kuroda, Warm Spraying: An Improved Spray Process to Deposit Novel Coatings, *Surf. Coat. Technol.*, 2008, **202**(18), p 4369–4373.

26. J. Sienkiewicz, S. Kuroda, H. Murakami, H. Araki, M. Giżyński and K.J. Kurzydłowski, Microstructure and Oxidation Performance of TiAl-(Cr, Nb, Ta) Coatings Fabricated by Warm Spray and High-Velocity Oxy-Fuel Spraying, *J. Therm. Spray Technol.*, 2019, **28**(3), p 563–579.

27. H. Tabbara, S. Gu and D.G. McCartney, Computational Modelling of Titanium Particles in Warm Spray, *Comput. Fluids*, 2011, **44**(1), p 358–368.

28. P. Chivavibul, M. Watanabe, S. Kuroda, J. Kawakita, M. Komatsu, K. Sato and J. Kitamura, Effect of Powder

29. T. Mori, S. Kuroda, H. Murakami, H. Katanoda, Y. Sakamoto and S. Newman, Effects of Initial Oxidation on β Phase Depletion and Oxidation of CoNiCrAlY Bond Coatings Fabricated by Warm Spray and HVOF Processes, *Surf. Coat. Technol.*, 2013, **221**, p 59–69.

30. T. Varis, T. Suhonen, J. Laakso, M. Jokipii and P. Vuoristo, Evaluation of Residual Stresses and Their Influence on Cavitation Erosion Resistance of High Kinetic HVOF and HVAF-Sprayed WC-CoCr Coatings, *J. Therm. Spray Technol.*, 2020, **29**(6), p 1365–1381.

31. J. Gutleber, R. Molz, J. He, C. Weber, and J. Colmenares, "New Developments in HVOF Spraying for Internal Diameter Coatings," *Proceedings of the Conference*, (Düsseldorf, Germany), DVS Media GmbH, Düsseldorf, 2017, p 501–504.

32. J. Pulsford, F. Venturi, Z. Pala, S. Kamnis and T. Hussain, Application of HVOF WC-Co-Cr Coatings on the Internal Surface of Small Cylinders: Effect of Internal Diameter on the Wear Resistance, *Wear*, 2019, **432–433**, p 202965.

33. J. Pulsford, S. Kamnis, J. Murray, M. Bai and T. Hussain, Effect of Particle and Carbide Grain Sizes on a HVOAF WC-Co-Cr Coating for the Future Application on Internal Surfaces: Microstructure and Wear, *J. Therm. Spray Technol.*, 2018, **27**(1–2), p 207–219.

34. F.E. Marble, Dynamics of a Gas Containing Small Solid Particles, *Combustion and Propulsion (5th AGARDograph Colloquium)*, (New York), Pergamon Press, 1963, p 175–213, https://resolver.caltech.edu/CaltechAUTHORS:20110208-103139308. Accessed 22 March 2020.

35. A. Amado, M. Schmid, G. Levy, and K. Wegener, Advances in SLS Powder Characterization, *22nd Annu. Int. Solid Free. Fabr. Symp.—Addit. Manuf. Conf. SFF 2011*, 2011.

36. A. Spierings, M. Voegtlin, T. Bauer, and K. Wegener, Powder Flowability Characterisation Methodology for Powder-Bed-Based Metal Additive Manufacturing, *Prog. Addit. Manuf.*, 2015.

37. W. Tillmann, C. Schaak, and B. Krekler, "Investigation of the Powder Feeding Behavior of Different WC-Co(Cr) Powders for ID Applications," *ITSC 2019—Proceedings of the International Thermal Spray Conference*, F. Azarmi, J. Lau, J. Veilleux, C. Widener, F. Toma, H. Koivuluoto, K. Balani, Hi. Li, and K. Shinoda, Eds., (Yokohama, Japan), ASM International, Materials Park, OH, USA, 2019, p 571–577.

38. G. Matthäus, "Anwendungen Für HVOF Und Plasmabeschichtungen Auf Basis Ultrafeiner Pulver < 10 Mm [Applications for HVOF and Plasma Coatings Based on Ultra-Fine Powders <10 Mm]," *Tagungsunterlagen*, (Erding (Germany)), Gemeinschaft Thermisches Spritzen e.V. (GTS), Unterschleißheim, Deutschland, 2018, p 73–82.

39. G. Mauer, R. Vaßen and D. Stöver, Comparison and Applications of DPV-2000 and Accuraspray-G3 Diagnostic Systems, *J. Therm. Spray Technol.*, 2007, **16**(3), p 414–424.

40. D.K. Shetty, I.G. Wright, P.N. Mincer and A.H. Clauer, Indentation Fracture of WC-Co Cermets, *J. Mater. Sci.*, 1985, **20**(5), p 1873–1882.

41. D.K. Shetty and I.G. Wright, On Estimating Fracture Toughness of Cemented Carbides from Palmqvist Crack Sizes, *J. Mater. Sci. Lett.*, 1986, **5**(3), p 365–368.

42. M. Watanabe, C. Brauns, M. Komatsu, S. Kuroda, F. Gärtner, T. Klassen and H. Katanoda, Effect of Nitrogen Flow Rate on Microstructures and Mechanical Properties of Metallic Coatings by Warm Spray Deposition, *Surf. Coat. Technol.*, 2013, **232**, p 587–599.

43. S. Kuroda, M. Watanabe, K. Kim and H. Katanoda, Current Status and Future Prospects of Warm Spray Technology, *J. Therm. Spray Technol.*, 2011, **20**(4), p 653–676.

44. R.M. Molak, H. Araki, M. Watanabe, H. Katanoda, N. Ohno and S. Kuroda, Warm Spray Forming of Ti-6Al-4V, *J. Therm. Spray Technol.*, 2014, **23**(1–2), p 197–212.

45. X. Guo, M.-P. Planche, J. Chen and H. Liao, Relationships between In-Flight Particle Characteristics and Properties of HVOF Sprayed WC-CoCr Coatings, *J. Mater. Process. Technol.*, 2014, **214**(2), p 456–461.

46. L. Zhao, M. Maurer, F. Fischer and E. Lugscheider, Study of HVOF Spraying of WC–CoCr Using On-Line Particle Monitoring, *Surf. Coat. Technol.*, 2004, **185**(2–3), p 160–165.

47. M. Li and P.D. Christofides, Multi-scale Modeling and Analysis of an Industrial HVOF Thermal Spray Process, *Chem. Eng. Sci.*, 2005, **60**(13), p 3649–3669.

48. M. Li and P.D. Christofides, Computational Study of Particle In-Flight Behavior in the HVOF Thermal Spray Process, *Chem. Eng. Sci.*, 2006, **61**(19), p 6540–6552.

49. M. Li, D. Shi and P.D. Christofides, Modeling and Control of HVOF Thermal Spray Processing of WC-Co Coatings, *Powder Technol.*, 2005, **156**(2–3), p 177–194.

50. T.C. Hanson and G.S. Settles, Particle Temperature and Velocity Effects on the Porosity and Oxidation of an HVOF Corrosion-Control Coating, *J. Therm. Spray Technol.*, 2003, **12**(3), p 403–415.

51. T.C. Hanson, C.M. Hackett and G.S. Settles, Independent Control of HVOF Particle Velocity and Temperature, *J. Therm. Spray Technol.*, 2002, **11**(1), p 75–85.

52. T.C. Totemeier, R.N. Wright and W.D. Swank, Microstructure and Stresses in HVOF Sprayed Iron Aluminide Coatings, *J. Therm. Spray Technol.*, 2002, **11**(3), p 400–408.

53. J. Gutleber and J. Tewes, "Neuartige HVOF-Technologie für das Beschichten kleiner Innendurchmesser [Novel HVOF Technology for Small ID Spraying]," *Conference proceedings*, (Erding), Gemeinschaft Thermisches Spritzen e.V. (GTS), Unterschleißheim, Deutschland, 2018, p 123–132.

54. J. Pan, S. Hu, L. Yang, K. Ding and B. Ma, Numerical Analysis of Flame and Particle Behavior in an HVOF Thermal Spray Process, *Mater. Des.*, 2016, **96**, p 370–376.

55. I. Baumann, L. Hagen, W. Tillmann, P. Hollingsworth, D. Stangier, G. Schmidtmann, M. Tolan, M. Paulus and C. Sternemann, Process Characteristics, Particle Behavior and Coating Properties during HVOF Spraying of Conventional, Fine and Nanostructured WC-12Co Powders, *Surf. Coat. Technol.*, 2021, **405**, p 126716.

56. K. Kim, M. Watanabe, J. Kawakita and S. Kuroda, Effects of Temperature of In-Flight Particles on Bonding and Microstructure in Warm-Sprayed Titanium Deposits, *J. Therm. Spray Technol.*, 2009, **18**(3), p 392–400.

57. E. Dongmo, M. Wenzelburger and R. Gadow, Analysis and Optimization of the HVOF Process by Combined Experimental and Numerical Approaches, *Surf. Coat. Technol.*, 2008, **202**(18), p 4470–4478.

58. A.G.M. Pukasiewicz, H.E. de Boer, G.B. Sucharski, R.F. Vaz and L.A.J. Procopiak, The Influence of HVOF Spraying Parameters on the Microstructure, Residual Stress and Cavitation Resistance of FeMnCrSi Coatings, *Surf. Coat. Technol.*, 2017, **327**, p 158–166.

59. K. Bobzin, F. Ernst, J. Zwick and G. Matthäus, Analyse von Partikeleigenschaften Beim Thermischen Spritzen von Mikropulvern, *Mater. Sci. Eng. Technol.*, 2007, **38**, p 149–154.

60. J.A. Picas, M. Punset, M.T. Baile, E. Martín and A. Forn, Effect of Oxygen/Fuel Ratio on the in-Flight Particle Parameters and Properties of HVOF WC-CoCr Coatings, *Surf. Coat. Technol.*, 2011, **205**, p S364–S368.

61. S.-L. Zhang, C.-X. Li, C.-J. Li, G.-J. Yang, and M. Liu, Application of High Velocity Oxygen Fuel Flame (HVOF) Spraying to Fabrication of La0.8Sr0.2Ga0.8Mg0.2O3 Electrolyte for Solid Oxide Fuel Cells, *J. Power Sources*, 2016, **301**, p 62–71.

62. A. Killinger, P. Müller and R. Gadow, What Do We Know, What Are the Current Limitations of Suspension HVOF Spraying?, *J. Therm. Spray Technol.*, 2015, **24**, p 1130–1142.

63. S. Kamnis and S. Gu, Study of In-Flight and Impact Dynamics of Nonspherical Particles from HVOF Guns, *J. Therm. Spray Technol.*, 2010, **19**(1–2), p 31–41.

64. J. Pattison, S. Celotto, A. Khan and W. O'Neill, Standoff Distance and Bow Shock Phenomena in the Cold Spray Process, *Surf. Coat. Technol.*, 2008, **202**(8), p 1443–1454.

65. W. Tillmann, P. Hollingsworth, I. Baumann, M. Tolan, M. Paulus, and F. Wieland, "Nanostructured WC-Co Coatings Manufactured by Fine Powders (− 10 + 2 Mm) with Ultra-Fine Carbides (400 Nm) by Means of HVOF," *Conference proceedings*, (Hamburg), DVS Media GmbH, 2011.

66. I. Baumann, "Hochverschleissfeste Und Konturnahe Werkzeugoberflaechen Durch Hochgeschwindigkeitsflammspritzverfahren," Technische Universitaet Dortmund/Vulkan-Verlag Essen, 2012.

67. C.-J. Li and G.-J. Yang, Relationships between Feedstock Structure, Particle Parameter, Coating Deposition, Microstructure and Properties for Thermally Sprayed Conventional and Nanostructured WC–Co, *Int J. Refract. Met. Hard Mater.*, 2013, **39**, p 2–17.

68. Q. Zhan, L. Yu, F. Ye, Q. Xue and H. Li, Quantitative Evaluation of the Decarburization and Microstructure Evolution of WC–Co during Plasma Spraying, *Surf. Coat. Technol.*, 2012, **206**(19–20), p 4068–4074.

69. D.V. Suetin, I.R. Shein and A.L. Ivanovskii, Structural, Electronic and Magnetic Properties of η Carbides (Fe3W3C, Fe6W6C, Co3W3C and Co6W6C) from First Principles Calculations, *Phys. B Condens. Matter*, 2009, **404**(20), p 3544–3549.

70. Y. Li, Y. Gao, Z. Fan, B. Xiao, Q. Yue, T. Min and S. Ma, First-Principles Study on the Stability and Mechanical Property of Eta M3W3C (M = Fe Co, Ni) Compounds, *Phys. B Condens. Matter*, 2010, **405**(3), p 1011–1017.

71. Z.G. Ban and L.L. Shaw, Characterization of Thermal Sprayed Nanostructured WC-Co Coatings Derived From Nanocrystalline WC-18wt.%Co Powders, *J. Therm. Spray Technol.*, 2003, **12**(1), p 112–119.

72. W. Tillmann, I. Baumann, P. Hollingsworth and L. Hagen, Sliding and Rolling Wear Behavior of HVOF-Sprayed Coatings Derived from Conventional, Fine and Nanostructured WC-12Co Powders, *J. Therm. Spray. Technol.*, 2014, **23**, p 262–280.

73. J.M. Tarragó, D. Coureaux, Y. Torres, E. Jiménez-Piqué, L. Schneider, J. Fair and L. Llanes, Strength and Reliability of WC-Co Cemented Carbides: Understanding Microstructural Effects on the Basis of R-Curve Behavior and Fractography, *Int. J. Refract. Met. Hard Mater.*, 2018, **71**, p 221–226.

74. N. Ma, L. Guo, Z. Cheng, H. Wu, F. Ye and K. Zhang, Improvement on Mechanical Properties and Wear Resistance of HVOF Sprayed WC-12Co Coatings by Optimizing Feedstock Structure, *Appl. Surf. Sci.*, 2014, **320**, p 364–371.

75. P. Chivavibul, M. Watanabe, S. Kuroda and K. Shinoda, Effects of Carbide Size and Co Content on the Microstructure and Mechanical Properties of HVOF-Sprayed WC–Co Coatings, *Surf. Coat. Technol.*, 2007, **202**(3), p 509–521.

76. P. Mi, H. Zhao, T. Wang and F. Ye, Sliding Wear Behavior of HVOF Sprayed WC-(Nano-WC-Co) Coating at Elevated Temperatures, *Mater. Chem. Phys.*, 2018, **206**, p 1–6.